The role of mesoscale instabilities in the sting-jet dynamics of windstorm Tini

Received: 13 September 2017 | Revised: 26 January 2018 | Accepted: 13 February 2018

DOI: 10.1002/qj.3264

RESEARCH ARTICLE

Quarterly Journal of the Royal Meteorological Society RMetS

The role of mesoscale instabilities in the sting-jet dynamics of windstorm *Tini*

Ambrogio Volonté | Peter A. Clark | Suzanne L. Gray

Department of Meteorology, University of Reading, Reading, UK

Correspondence
Ambrogio Volonté, Department of Meteorology, University of Reading, Earley Gate, P.O. Box 243, Reading RG6 6BB, UK. Email: a.volonte@reading.ac.uk

Funding information
AXA Research Fund, "Sting Jet Windstorms in Current and Future Climates."

Sting jets (SJs) occur as an additional region of low-level strong winds in some Shapiro–Keyser-type extratropical cyclones. While SJs are widely accepted as being distinct from the warm and cold conveyor belts, the mechanisms responsible for their occurrence are still not fully understood. Here we determine the relative importance of the release of mesoscale instabilities and synoptic-scale cyclone dynamics, so addressing an area of current debate. Numerical weather prediction simulations of a SJ-containing windstorm are analysed and Lagrangian trajectories used to assess the evolution of, and mesoscale atmospheric instabilities (e.g. symmetric and inertial instabilities) in, the descending airstream. The SJ undergoes a two-stage descent: cooling via sublimation followed by a large acceleration accompanied by instability release. Combined tilting and stretching of vorticity play a major role in the local onset of instability on the airstream. Vorticity and frontogenesis fields have a narrow slantwise banded structure in the cloud head and around the SJ; the descending SJ modifies the widespread frontolysis expected from the large-scale dynamics alone in the frontal-fracture region. A coarser-resolution simulation also generates strong winds in the frontal-fracture region, although these are significantly weaker than in the higher-resolution simulation. The SJ airstream in the coarser-resolution simulation undergoes a weaker descent without instability generation and descends in a widespread frontolytic region. Hence, while the SJ undergoes a process of destabilisation that enhances its descent and acceleration in the higher-resolution simulation, enhancing the strong winds already generated by the synoptic-scale cyclone dynamics, this destabilisation does not occur in the SJ produced by a coarser-resolution simulation, resulting in weaker winds. This analysis reveals the synergy between the paradigms of SJ occurrence through the release of mesoscale instabilities and synoptic-scale cyclone dynamics and demonstrates that the current debate may in part be a consequence of the model resolutions used by different studies.

KEYWORDS
cyclone, extratropical, frontolysis, sting jet, symmetric instability, wind

1 | INTRODUCTION

The term "Sting Jet" (SJ) has gained rapid acceptance in the meteorological literature and by the media since it was first used by Browning (2004) to describe an observed mesoscale region of extremely strong surface winds distinct from the winds associated with the warm conveyor belt (WCB) and cold conveyor belt (CCB) in the extratropical cyclone that devastated southeast England on October 16, 1987. Climatological studies have revealed that SJs are likely to occur frequently in extratropical cyclones, although they may be the direct cause of the strongest surface winds

and gusts over land more rarely. For example, Hart *et al.* (2017) identified SJ (mesoscale instability-based) precursors in about a third of the more than 5000 North Atlantic cyclones tracked over 33 extended winters using data from the interim ECMWF reanalysis (ERA-Interim) and Hewson and Neu (2015) diagnosed that the strongest gusts over land in observed storms can frequently be attributed to the CCB and WCB, as well as the SJ (see their table 1). Despite increasing usage of this term (e.g. analysis in Schultz and Browning (2017)), the mechanisms leading to the generation and descent of the SJ are controversial. In this article we address this controversy through analysis of a case study that illustrates the co-existence of multiple mechanisms. In particular, we demonstrate (a) the complexity of mesoscale instability release that can contribute to the SJ and (b) that some of the debate in the literature likely results from the use of numerical models that have insufficient resolution to represent these mesoscale instabilities and their release.

Here we adopt the definition of a SJ proposed in the recent review by Clark and Gray (2018), which is very consistent with the description given by Schultz and Browning (2017):

> The SJ is defined as a coherent air flow that descends from mid-levels inside the cloud head into the frontal-fracture region of a Shapiro–Keyser cyclone over a period of a few hours leading to a distinct region of near-surface stronger winds. It therefore lies above the CCB during some stage in its life, but, at least in some cases, descends to reach the top of the boundary layer ahead of the CCB. It is not attributed to a specific mechanism in this definition.

The debate over the mechanisms leading to the generation and descent of the SJ revolves around the contributions of "large-scale" dynamics, mesoscale instability release, frontal dynamics and evaporative cooling. The currently analysed case is, to the authors' knowledge, the first case for which these mechanisms have been demonstrated to co-exist. These contributions are reviewed in Clark and Gray (2018) and summarized here.

"Large-scale dynamics" refers here to the balanced dynamics taking place within the cloud head and frontal-fracture region of cyclones (figure 1 of Martínez-Alvarado *et al.* (2014) shows a schematic illustrating the features found in intense extratropical cyclones). As recognised by Browning (2004), gradient wind balance is sufficient to account for a large part of the strength of the winds in the frontal-fracture region. Subsequent studies (Schultz and Sienkiewicz, 2013; Coronel *et al.*, 2016; Slater *et al.*, 2017) have demonstrated association between SJ-type airstreams and frontolysis, divergent $\mathbf{Q}$ vectors, and/or quasi-geostrophic omega. This body of work has established that downwards advection of strong winds by the frontolytical secondary circulation (implicitly found in the frontal-fracture region of a cyclone) followed by acceleration by the low-level pressure gradient can give rise to strong winds. Indeed, in simulations by models that are unable to resolve mesoscale features, these large-scale dynamical mechanisms are the only ones that can yield SJ-like features in cyclones.

Browning (2004) speculated that, due to the banded nature of the cloud head, the release of the mesoscale instability known as conditional symmetric instability (CSI) may have strengthened the SJ in the October 1987 storm (Schultz and Schumacher (1999) give a review of this and other mesoscale instabilities). Subsequent studies (Clark *et al.*, 2005; Gray *et al.*, 2011; Baker *et al.*, 2014; Martínez-Alvarado *et al.*, 2014) have provided evidence that mesoscale instability release (in particular of CSI, but also of conditional instability (CI), symmetric instability (SI) and inertial instability (II)) is associated with the presence and descent of the SJ in SJ storms. In contrast, other studies (e.g. the case study of windstorm *Ulli* from 2012 by Smart and Browning (2014)) have found no evidence of a strong contribution from CSI release.

Circulations associated with frontal dynamics cannot cleanly be distinguished from circulations associated with mesoscale instability release. For example, Xu (1989) demonstrate the spectrum of banded behaviour that can occur as the width of the frontal forcing is varied and the moist potential vorticity changes from positive to negative using an extended form of the Sawyer–Eliassen equation for frontal circulation (also section 4 in the review by Schultz and Schumacher, 1999). However, it seems likely that these frontal circulations can contribute to the SJ descent.

Finally, several studies have attempted to diagnose the contribution from the cooling necessarily associated with the evaporation of cloud as the SJ leaves the cloud head. While Clark *et al.* (2005) demonstrated a plausible contribution of evaporative cooling to the descent of the SJ in the October 1987 storm (with the SJ-airstream trajectories that descended the most exhibiting potential cooling of 3–8 K), other studies, in particular idealized modelling studies in which the effect of evaporative cooling has been diagnosed by turning it off (Baker *et al.*, 2014; Coronel *et al.*, 2016), have found little impact on the SJ strength or descent rate.

Model resolution is a key aspect when investigating the dynamics of mesoscale phenomena (such as SJs) that form part of evolving synoptic-scale weather systems such as extratropical cyclones. Baroclinic systems are generally dominated by shallow slantwise motions of order 1:100 (roughly $f : N$, where f is the Coriolis parameter and N the Brunt–Väisälä frequency). Systems with strong frontal dynamics and/or the release of CSI are often somewhat steeper (e.g. 1:50). Previous research has demonstrated that it is important to resolve the vertical spacing and aspect ratio of CSI-related circulations (Persson and Warner, 1993; Lean and Clark, 2003), which requires a grid spacing of 200–250 m in the lower mid-troposphere or better. With 1:50 slope this implies a horizontal spacing of around 10–12 km. In practice, the solution developed by the model tends to be dominated by the poorer

of the horizontal and the vertical resolution divided by the aspect ratio of the flow (so a 20 km horizontal grid simulating a flow with 1:50 aspect ratio tends to produce a solution similar to a model with 400 m vertical grid spacing, even if the actual spacing is smaller). Incidentally, if ice sublimation is important in the frontal dynamics of a system (as it often is), a similar resolution is required to capture the depth-scale of sublimation (Forbes and Clark, 2003). Previous simulations of SJs have shown that they descend out of the cloud head with roughly this (1:50) aspect ratio and have shallow vertical depth requiring a grid spacing of 200–250 m (Clark *et al.*, 2005; Gray *et al.*, 2011).

In this study we diagnose the role of mesoscale instabilities in a case study: windstorm *Tini*. This intense windstorm brought strong winds and gusts to the UK in February 2014 and satellite imagery and wind profiler observations show features consistent with a SJ. The rest of this article is structured as follows. The configuration of the numerical model simulations and the post-processing diagnostics (trajectory analysis and mesoscale instability characterisation) are described in section 2. The comparison of the high-resolution model simulation with observations, identification and characterisation of a SJ in the model simulation, evaluation of mesoscale instabilities along the SJ, and a comparison with results from a coarser resolution model are presented in section 3. The last subsection contains a comparison with a coarser model simulation; this comparison is included to reconcile our results, which show a clear contribution of mesoscale instability release to the generation and descent of the SJ in windstorm *Tini*, with the results of other studies that have concluded that this mechanism does not contribute. In particular, Slater *et al.* (2017) also show results from a simulation of windstorm *Tini*, but attribute the SJ-like feature to large-scale dynamics. Since their simulation used a resolution that is too coarse to resolve mesoscale instability release, this part of our study addresses the role that model resolution has on the diagnosed contributions of mechanisms to SJs. Discussion and conclusions are presented in section 4. Although our results are drawn from a single case study, their consistency with those from other studies enables us to make broad conclusions regarding the contribution of mesoscale instability release to SJ generation and descent in extratropical cyclones as well as the potential limitation of simulating these storms with insufficient model resolution.

2 | METHODS

2.1 | Numerical weather prediction model simulations

Extratropical cyclone *Tini* has been simulated using the MetUM version 8.2, as used by Hart *et al.* (2015). The MetUM is a finite-difference model which solves the non-hydrostatic deep atmosphere dynamical equations. The integration scheme is semi-implicit and semi-Lagrangian (Davies *et al.*, 2005). The model uses Arakawa C staggering in the horizontal (Arakawa and Lamb, 1977) and a terrain-following hybrid-height Charney–Phillips vertical coordinate (Charney and Phillips, 1953). Model parametrizations include long-wave and short-wave radiation (Edwards and Slingo, 1996), boundary-layer mixing (Lock *et al.*, 2000), cloud microphysics and large-scale precipitation (Wilson and Ballard, 1999) and convection (Gregory and Rowntree, 1990).

The simulations (technically hindcasts) were performed with two different resolutions and domains. The first hindcast used a global domain, comprising 1024×769 horizontal grid points, with horizontal grid spacing around 26 km at midlatitudes. 70 vertical levels were used (as in the operational global model) with the top level around 80 km and spacing smoothly stretching from the surface, ranging from around 170–280 m at heights between 1 and 3 km to around 280–350 m between 3 and 5 km. Initial conditions for the global simulation were given by the Met Office operational analysis valid at 1200 UTC on February 11, 2014. The global domain provided initial and lateral boundary conditions (every 3 hr) for a limited-area model that produced the second hindcast. This limited-area domain covers the same area as the Met Office's recently operational North Atlantic and European (NAE) domain model, with the same horizontal resolution but a different vertical level set used to provide higher vertical resolution. The horizontal grid spacing was 0.11° (∼12 km) in both longitude and latitude on a rotated grid centred around 52.5°N, 2.5°W. The NAE domain extends approximately from 30°N to 70°N in latitude and from 60°W to 40°E in longitude. A set of 70 vertical levels with a top level of 40 km was used; these levels are the same ones as used in the 1.5 km horizontal grid spacing operational UK Variable resolution (UKV) model. (However, note that we do not perform a simulation with the UKV model as the domain is too small to capture the cyclone evolution). Vertical spacing gradually stretches from around 120–200 m at heights between 1 and 3 km to around 200–260 m between 3 and 5 km. This resolution is considered sufficient for the representation of SJs based on previous studies (section 1).

The primary purpose of the global simulation was to drive the limited-area model. However, it has also been used to test the sensitivity of the results to horizontal and vertical resolution in section 3.4 (all other sections show results only from the limited-area model). The 26 km horizontal grid spacing of the global model is insufficient to represent the horizontal scale of many SJs reported in the literature. Both the global simulation and the limited-area simulation conform (approximately) to the 1:50 aspect ratio required to represent sloping SJs, but the global model resolution does not completely meet the required vertical resolution criterion of 200–250 m grid spacing (section 1). Hence, we have two simulations: one that we anticipate adequately resolves SJs and the other that we anticipate will not. Initial runs were also performed using the limited-area domain, but with the global model level set. This resulted in a simulation, as expected, closer to the

global simulation. Results are not reported here as they merely confirm that intermediate behaviours occur.

Model data were interpolated onto pressure levels with 15 hPa spacing for both model configurations before calculating the diagnostics and performing the Lagrangian analysis described in the next subsection. The pressure spacing is similar to the one between limited-area model levels in the mid-low troposphere, and comparisons between the interpolated data and the original model-level data confirm that no significant degradation occurred through this interpolation process.

2.2 | Trajectory analysis

Lagrangian trajectories have been used extensively in SJ research (e.g. Clark *et al.*, 2005; Baker *et al.*, 2014; Martínez-Alvarado *et al.*, 2014; Smart and Browning, 2014). Indeed, Schultz and Browning (2017) emphasise that "definitive evidence of the existence of the sting jet requires trajectories and/or other diagnostics." It is possible in a Lagrangian framework to isolate airstreams and assess their properties and their evolution in time. In this study, trajectories were computed using the LAGRANTO Lagrangian analysis tool (Wernli and Davies, 1997; Sprenger and Wernli, 2015). LAGRANTO uses an iterative Euler scheme with an iteration step equal to 1/12 of the time spacing of input data. Ideally, data every model time step (2.5 min for the higher-resolution simulation) would be used to compute the trajectories, but in practice some compromise is necessary, and acceptable, to reduce the amount of output required from the model. It was found that trajectories computed with input frequency of model data of 15 min (i.e. six model time steps), showed a marked improvement in their quality compared with hourly-input data, and yielded satisfactory conservation of relevant physical quantities such as wet-bulb potential temperature (θ_w); hence, all the results referring to the higher-resolution simulation use this input frequency (while trajectories are computed with an hourly input frequency in the coarser-resolution simulation).

2.3 | Atmospheric instability diagnostics

An objective of this article is to evaluate the role of mesoscale instabilities in the generation of the SJ simulated in *Tini*. The method followed here to detect these atmospheric instabilities on the SJ airstream follows that presented in Martínez-Alvarado *et al.* (2014). The criteria for labelling are shown in Table 1. Diagnostics for each instability are evaluated at each grid point and interpolated onto relevant trajectories. The additional constraint for the two conditional instabilities (CI and CSI) of $RH_{ice} > 80\%$ (where RH_{ice} is relative humidity calculated with respect to ice) is used because these instabilities can only be released if the air is saturated. In the model, partial cloud formation occurs when RH exceeds a certain threshold: 80% in the free troposphere. A slightly more accurate diagnostic could probably be designed, but in practice regions identified with these instabilities at this RH are contiguous with similar cloudy regions that are close to saturated. Grid points where the diagnostic tests for CSI or CI indicate instability but the saturation constraint is not met are not labelled as stable (S), and do not belong to any of the categories in Table 1. A grid point is labelled as stable only if none of the four diagnostic tests indicate instability.

TABLE 1 Criteria for trajectory instability and stability labels

Label	N_m^2	RH_{ice}	ζ_z	*PV*	*MPV**
Conditional Instability (CI)	< 0	$> 80\%$			
Inertial Instability (II)			< 0		
Symmetric Instability (SI)				< 0	
Conditional Symmetric Instability (CSI)		$> 80\%$			< 0
Stable	≥ 0		≥ 0	≥ 0	≥ 0

N_m^2 is the moist Brunt–Väisälä frequency as defined by Durran and Klemp (1982). ζ_z is the vertical component of absolute vorticity (on pressure levels). PV is the potential vorticity and *MPV** the moist saturated potential vorticity (Bennetts and Hoskins, 1979). Multiple entries in a row require all criteria to be satisfied (i.e. "and" rather than "or").

Every point can be labelled with more than one instability at the same time if two or more conditions are met. It should be borne in mind that the underlying theory for each of these instabilities relies on assumptions regarding the background state upon which perturbations grow: uniform flow for CI, uniform potential vorticity (PV) for CSI, and barotropic atmosphere for II. These conditions are rarely met in practice and are certainly not met in an intense cyclone such as *Tini* where strong pressure gradients, wind shears and PV gradients occur. Our approach is to take these criteria as indicators of the underlying atmospheric state to highlight the processes leading to instabilities that might drive the dynamics of the SJ. For example, a formal definition of CSI states that a point is only defined having CSI if II and CI are absent (Schultz and Schumacher, 1999). However, we have labelled points with CSI if $MPV^* < 0$ even when SI and II are present; as will be shown, this provides useful insight into the whole period when MPV^* is negative in a nearly saturated environment, even though the contemporary presence of SI and/or II means that we would interpret any release of instability as due to the latter rather than slantwise convection induced by CSI release. Likewise, SI and II can be present at the same time. Arguably, in most circumstances, SI and II are the same thing, and would be labelled as SI (with II reserved for barotropic flow), but we have kept both to keep track, in particular, of the vorticity.

While PV can be related most simply to the absolute vorticity on potential temperature (θ) surfaces, it is evident that the θ surfaces are undergoing quite substantial deformation in the region of the SJ. Ertel's theorem tells us about conservation of PV, and the nature of sources and sinks. In many cases, PV is changed by diabatic processes through changes in static stability. The change in PV occurs through adjustment

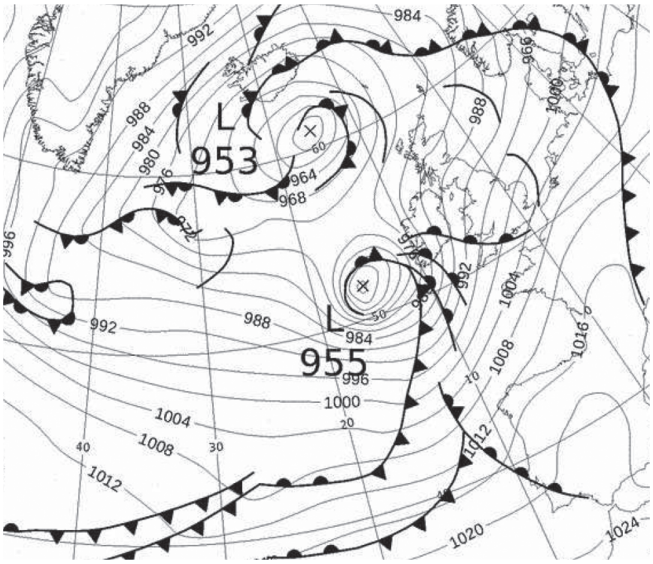

FIGURE 1 Adapted from the Met Office analysis chart valid at 0600 UTC on February 12, 2014 showing windstorm *Tini* approaching Ireland from the west. Figure archived by http://www1.wetter3.de. UK Crown copyright

to a balanced flow. The adjustment process requires time that may be similar to, or even longer than, the process generating the change in PV. Therefore we cannot assume a perfectly adjusted flow (only, in the case of negative PV, the lack of existence of one). On the other hand, direct changes to vorticity (which may well be occurring as part of the adjustment process) are more straightforward to analyse, at least kinematically. In particular, where diabatic processes generate negative PV due to negative static stability, it is likely that vertical turbulent convection rapidly removes the resulting instability before there is any impact on the vorticity. Where negative PV is produced and persists on an air parcel, this is most likely due to the indirect effect of diabatic processes tilting the horizontal component of vorticity.

3 | RESULTS

3.1 | Synoptic development of the model simulation compared to observations

3.1.1 | Background

Windstorm *Tini* (Figure 1) was one of the many intense extratropical cyclones that passed over the British Isles during winter 2013–2014, the stormiest winter on record in the UK according to Matthews *et al.* (2014). *Tini* was arguably the most severe of all those intense cyclones, with the analysed surface pressure minimum dropping 40 hPa in 18 hr between 1200 UTC on February 11, and 0600 UTC on February 12. This deepening rate is more than twice the 24 hPa (24 hr)$^{-1}$ threshold (at 60°N) used to define "extratropical bombs" (Sanders and Gyakum, 1980). The storm particularly affected coastal areas of northwest England and Wales: a Met Office red alert warning for wind was issued for these regions. Wind gusts were recorded to be close to record values reaching 94 kt (108 mph) at Aberdaron (Gwynedd), 83 kt (96 mph) at Lake Vyrnwy (Powys) and 81 kt (93 mph) at Capel Curig (Gwynedd), all in Wales. According to the Met Office, *Tini* was thus one of the most intense storms to affect Wales and northwest England in recent decades (http://www.metoffice.gov.uk/climate/uk/interesting/2014-janwind).

3.1.2 | Satellite imagery

Satellite imagery shows an evolution compatible with the Shapiro–Keyser conceptual cyclone model (Shapiro and Keyser, 1990). A prominent cloud head formed during the cyclone-deepening stage, leading to the formation of a well-defined bent-back front. Some "finger-shaped" cloud bands at the southern end of the cloud head occurred for a short period (approximately between 0400 and 0800 UTC on February 12, 2014) corresponding to the transition between stage II and stage III of the Shapiro–Keyser cyclone evolution. Figure 2a shows the cyclone structure at 0600 UTC, in the middle of this period. Similar banded structures at the cloud-head tip have been observed in SJ storms and linked to the multiple slantwise circulations associated with the release of CSI or similar mesoscale instabilities in the region (Browning and Field, 2004; Parton *et al.*, 2009). Figure 2c is at 1200 UTC, when the storm is in its mature stage IV as the bent-back front has wrapped around the cyclone centre and a warm seclusion has formed.

The limited-area model simulation follows a very similar pattern to the satellite imagery, with remarkably similar timing given the rapid development of the system. Figure 2b,d show simulated satellite images at 0600 and 1200 UTC on February 12, 2014 (18 and 24 hr into the forecast, respectively) using broadband outgoing long-wave radiation from the model radiation scheme. The similarities to the observed images in Figure 2a,c are evident. The simulation is not only capturing well the broad structure of the weather system and its overall location, but also some smaller-scale features. In particular, Figure 2b shows some cloud bands at the tip of the cloud head, resembling the banding observed in the actual satellite imagery. The ability of our model simulation to resolve this feature is dependent on vertical resolution: bands are only visible in the simulation with increased vertical resolution, i.e. using the UKV and not the operational global model vertical levels (section 2.1 gives details).

3.1.3 | Observations from the MST radar

The Mesosphere–Stratosphere–Troposphere radar wind profiler (NERC, 2017) is located at Capel Dewi (52.42°N, 4.01°W) near Aberystwyth, Wales (Figure 2b, d). This location is just south of the path followed by the cyclone centre. The recorded time series of wind speed is shown in Figure 3a. This time series can be thought of as similar to a west to east cross-section through the storm, with time displayed from right to left to facilitate interpretation, with the caveat that the

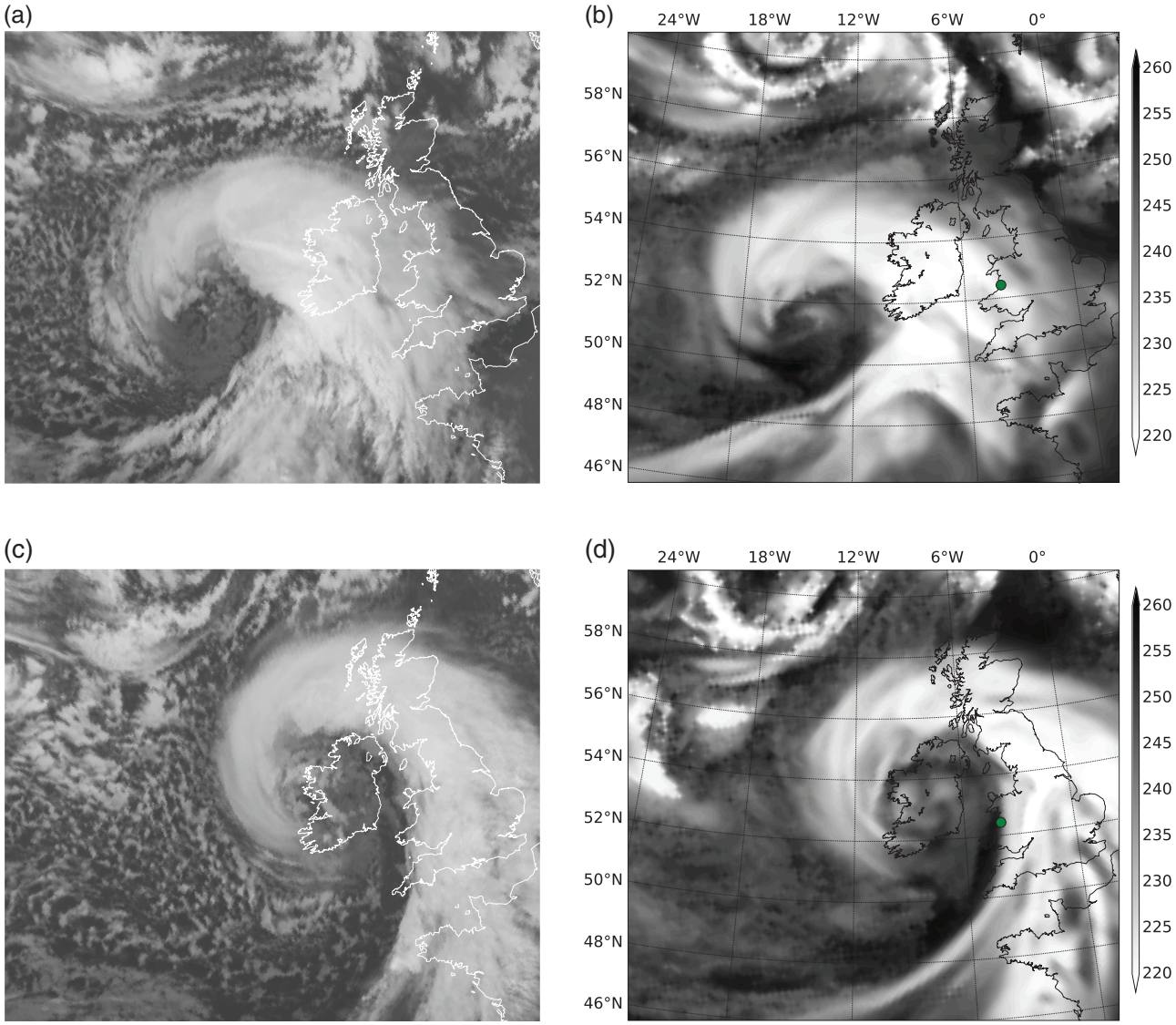

FIGURE 2 (a,c) observed and (b,d) simulated (using model outgoing long-wave brightness temperature (K)) satellite infrared imagery of windstorm *Tini* at (a,b) 0600 UTC and (c,d) 1200 UTC on February 12, 2014. (Satellite imagery from Meteosat Second Generation, image courtesy of Met Office and EUMETSAT). The green dot in (b) and (d) indicates the location of the Aberystwyth MST radar [Colour figure can be viewed at wileyonlinelibrary.com]

storm was developing during this period. Nevertheless, many of the key features of the storm can be identified.

Figure 3a shows strong winds in the upper troposphere (the upper-level jet) in the first half of the day signalling the arrival of the weather system. From around 0900 UTC, winds exceeding 35 m/s extend to the rest of the troposphere indicating what is probably the warm conveyor belt (WCB). During the passage of the cold front, after around 1200 UTC, strong winds become widespread in the whole troposphere. There is also an indication of tropopause folding between 1400 and 1500 UTC, in the form of a weak-speed descending tongue. The maximum in wind speed at around 3–5 km height visible just after the frontal passage has been suspected to be related to be a SJ (G. Parton, 2014; Personal communication). Its position compares well with the tip of the cloud head passing over the MST radar site and with the observed cloud striations and rain bands consistent with slantwise convection.

Figure 3b shows an equivalent time–height profile of wind speed from the limited-area simulation. Also shown are the θ_w in the troposphere and the height of the 2 PVU surface (the dynamical tropopause, where PVU = potential vorticity units). Though the timing is perhaps an hour different, with the simulation ahead of the observations, the figure shows considerable correspondence with the observations, particularly in the passage of the cold front, indicated by a sharp decrease in θ_w below 4 km height around 1200 UTC (in the model simulation), followed by tropopause folding associated with the fall of the 2-PVU tropopause down to 4 km height and with a weak-speed descending tongue. Comparing with horizontal plots from the model, it is possible to distinguish three different regions of low-level strong winds passing over the radar location. In time order, the first region visible in the plot, around 1000 UTC at around 2–4 km height associated with an extension down to the lower troposphere of the upper-level jet, is part of the WCB. It is located ahead of

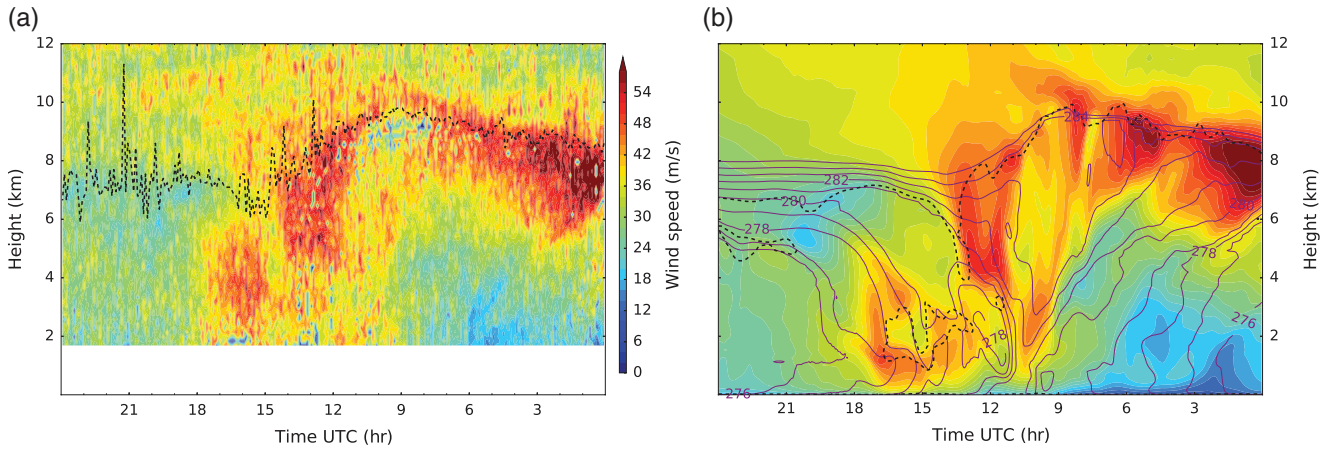

FIGURE 3 (a) Time–height plot of Aberystwyth MST radar on February 12, 2014 showing Doppler wind speed (colour shading), with black dashed line showing the radar-derived tropopause altitude. (b) Simulated time–height plot of Aberystwyth radar on the same day showing wind speed (shading), θ_w (purple contours, up to 285 K), and the height of 2 PVU surface (black dashed line) [Colour figure can be viewed at wileyonlinelibrary.com]

the cold front, with warm values of θ_w and with weak static stability above it. The last region, visible after 1500 UTC and characterized by values of θ_w lower than 278 K, can be attributed to the cold conveyor belt (CCB). Between 1200 and 1500 UTC is a wind maximum below 3 km height characterized by θ_w ranging from 278 to 280 K (with a possible extension to 3–4 km height between 1500 and 1700 UTC). The cold front passed at 1200 UTC and the bent-back front did not reach the Welsh coast before 1500 UTC, so this wind maximum was located in the frontal-fracture region and is attributable to the remnant of the already-descended SJ (given the appearance of bands in the cloud head around 8–10 hr earlier). Note that the modelled peak wind speed in this region seems to be in reasonably close agreement with the observations, peaking roughly in the range 45–50 m/s, even though, as will be shown below, the peak modelled wind speed earlier (and slightly further south) approached 60 m/s.

To summarize, the synoptic evolution and mesoscale structure of the limited-area simulation shows a strong, though not perfect, correspondence with the limited observations available. Both observations and simulations suggest the presence of a SJ, even though the lack of observational data below 2 km height does not allow us to verify that the wind maximum identified as a "suspected SJ" in the observations corresponds to its simulated counterpart rather than to the simulated CCB, given its late arrival. A more detailed analysis is necessary to assess if a SJ is actually present in the model simulation. This has been done in an Eulerian framework, investigating strong wind regions and θ_w patterns, and in a Lagrangian sense, identifying a suspected SJ airstream and looking at its properties and evolution along trajectories.

3.2 | Identification and characterization of a SJ in *Tini*

3.2.1 | Strong-wind regions

Figure 4 summarizes the cyclone structure in the limited-area simulation at 0700 UTC, the time when the strongest winds occurred at 850 hPa. Figure 4a,b show the cloud head wrapping around the cyclone centre. Note that a second, more broken, band of cloud wraps around the cyclone centre running from the west coast of Scotland to the tip of the cloud head. This suggests a second band of ascent. This is also the period during which bands are visible at the cloud-head tip in simulated imagery (cf. Figure 2). Moist isentropes (i.e. θ_w contours) highlight the position of the fronts in the system. The warm front is crossing the southern part of Ireland. The primary cold front is located south of it, orientated in a southwest–northeast direction and marking the western boundary of the warm-sector cloud. The bent-back front is evident to the west of the system, along with a warm seclusion represented by the 280 K contour; this seclusion is more clearly present at lower levels. The frontal-fracture region is indicated by an area of weak θ_w gradients, with the moist isentropes spreading out between the tip of the cloud head and the cold front. Comparing the location of these features with the pattern of strong winds, it is possible to identify the WCB on the eastern side of the cold front, centred around (9.5°W, 50°N), with winds reaching 48 m/s at 850 hPa. There is a much stronger wind maximum in the frontal-fracture region (13.5°W, 50°N), very focused and approaching 60 m/s that we identify as the SJ (details below in the rest of this section).

During its deepening stages, the cyclone travels over the Atlantic at an average speed of around 25 m/s; we estimated this speed by tracking the location of the sea-level pressure minimum. The motion is close to zonal (with the magnitude of meridional wind well below 5 m/s) until 0700 UTC. During the latter stages of cyclone evolution, not relevant for SJ generation and descent, the cyclone speed decreases and the direction turns towards the northwest. Due to this rapid cyclone motion, wind features like the CCB, mostly located on the northeastern side of the cyclone, are not evident in an Earth-relative frame of reference. Subtracting this motion from the Earth-relative wind, we obtain system-relative wind speed (Figure 4b). The CCB is very clearly visible in this reference frame wrapping around the cyclone centre to its north and west and located inside the cloud-head region. The

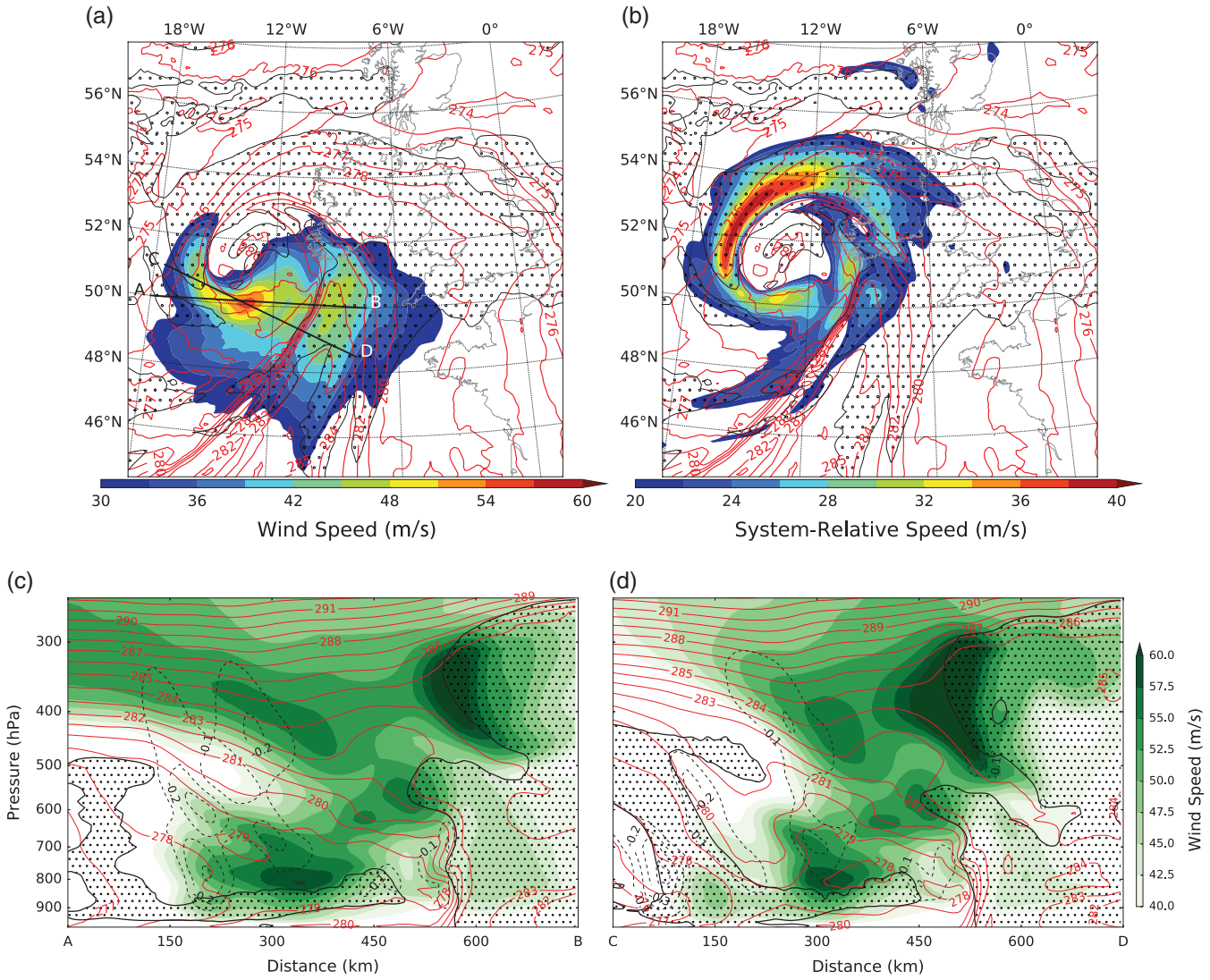

FIGURE 4 (a) Wind speed at 850 hPa (shading, m/s), θ_w at 850 hPa (K, red contours) and cloudy regions at 700 hPa (RH_{ice} >80%, black contour enclosing stippled regions). (b) is as (a), but with system-relative wind speed. (c, d) cross-sections (transects AB and CD respectively in (a)) of wind speed (green shading, m/s), negative vertical velocity (dashed black contours, m/s), θ_w (red contours, K) and cloudy regions (RH_{ice} >80%, thick black contour enclosing stippled regions). All plots are for 0700 UTC on February 12, 2014 [Colour figure can be viewed at wileyonlinelibrary.com]

previously identified wind maximum to the south of the system centre is clearly weaker in this reference frame, but also clearly distinct from the CCB. Given this distinction and its location, we identify the wind maximum to the south of the system centre as likely to be a SJ, subject to confirmation by trajectory analysis in the next section.

Figure 4c,d show two cross-sections that pass through the SJ wind maximum and the frontal fracture region. There is a broad resemblance to Figure 3. Though the latter is not a strict cross-section, as it is a fixed-space instead of a fixed-time section, the same general features can be identified. Both cross-sections show the upper-level jet located between 300 and 500 hPa, with its core exceeding 60 m/s at the edge of the warm-sector cloud. The WCB is visible underneath it on the warm side of the cold front, centred around 700 hPa and with winds exceeding 45 m/s. The mid-level wind maximum close to 60 m/s, located around 600 hPa, is possibly related to the dry-air intrusion (as defined by e.g. Browning and Roberts (1994)). The leading edge of the CCB is visible below 800 hPa on the left side of Figure 4d, with θ_w lines showing the separation between its 45 m/s peak winds and the warmer air in the frontal-fracture region. The intense wind maximum centred around 800 hPa in the frontal-fracture region in both cross-sections, identified as the SJ, reaches 60 m/s, stronger than the maximum at mid-levels and comparable with the upper-level jet. A weaker wind maximum centred at 700 hPa, but contiguous with the lower maxima, may be a secondary SJ. However, there is no obvious connection from the SJ(s) to the high-momentum air above. The jet is located just beneath some slanted isentropes, in an area with very weak θ_w gradients, where isentropes have undergone folding or buckling, as Figure 4d shows. It is also close to and "downstream of" (based on the isentropic slope) maxima of negative vertical velocity, particularly visible in Figure 4c. Note also two regions of slantwise descent (either side of the main cloud-head cloud) at the western end of Figure 4d, one

above the CCB, the other to the west of it. The second band of cloud discussed above that wraps around the cyclone centre outside the CCB is evident in Figure 4c to the west of the SJ in a location outside the more western region of strong slantwise descent.

Overall, we interpret these cross-sections as indication that the wind maximum results from the acceleration of a jet (i.e. the SJ) descending out of the cloud head. In the next section, we confirm this through the use of back-trajectories.

3.2.2 | Selection of trajectories

It is important to distinguish the SJ from the CCB and so Lagrangian trajectories have been used to follow the evolution of both. Figure 4a,b show the 850 hPa level, in order to highlight both the CCB and SJ flows, but the cross-sections in Figure 4c,d show that the maximum wind speed in the SJ is located at around 820 hPa. The grid points with wind speed exceeding 57 m/s at 0700 UTC located at 820 hPa or in contiguous levels (i.e. aligned vertically with the grid points selected at 820 hPa to form uninterrupted columns of points with speed exceeding the threshold) are selected as starting points for SJ trajectories. This methodology has been used to select a volume of trajectories belonging to the low-level wind maximum highlighted previously and to exclude any higher-level separate maxima. Trajectories from these selected points show strong descent, but with a variety of starting altitudes. However, at the core is a substantial set of trajectories descending from above 650 hPa. To focus on this maximally descending core, we show below the properties of the set of 52 trajectories located at a pressure smaller than 650 hPa at 0200 UTC and descending by more than 100 hPa between 0400 and 0600 UTC. This selection does not qualitatively change our conclusions, but it does make them clearer. The excluded trajectories appear to form the boundaries of the SJ and did not go through the whole process of descent. Starting points for CCB trajectories have been selected with the same methodology considering a threshold of 51 m/s centred at 820 hPa and evaluated at 1000 UTC, when the leading edge of CCB airstream is oriented in the same direction as the storm motion. In this later stage of the storm evolution, the strongest low-levels winds belong to the CCB and there is no longer an indication of a SJ.

Figure 5 shows a 3D visualization of system-relative trajectories related to the SJ and CCB for 9 hr during the most intense phase of evolution of the storm. It shows that the SJ and CCB airstreams represent different airmasses, each one undergoing its own evolution. The CCB stays at low levels and increases its RH_{ice} gradually, eventually becoming saturated while wrapping around the cyclone centre beneath the cloud head. The SJ trajectories instead start at about 700–800 hPa in the northern sector of the storm, enter into the cloud head rising up to 600 hPa, and later exit from its tip descending into the frontal-fracture region and drying out. Thus, the SJ is not an appendix of the CCB or its foremost part: the two airstreams are distinct and originate and evolve in two clearly different ways, as first described by Clark *et al.* (2005). A video animation (Figure S1) of the evolution of the (Earth-relative) trajectories showing the dynamics just presented can be found in the supplementary information. This animation highlights the relationship between the SJ descent and the increase of wind speed at 850 hPa at around 0600–0700 UTC and also the weaker wind maximum associated with the CCB at around 0900–1000 UTC. In the rest of this study we focus on the SJ airstream, characterising it by analysing time series of relevant physical quantities along its trajectories.

3.2.3 | Evolution of physical quantities along trajectories

Figure 6 shows the evolution of various physical quantities along the SJ-core trajectories identified as described above.

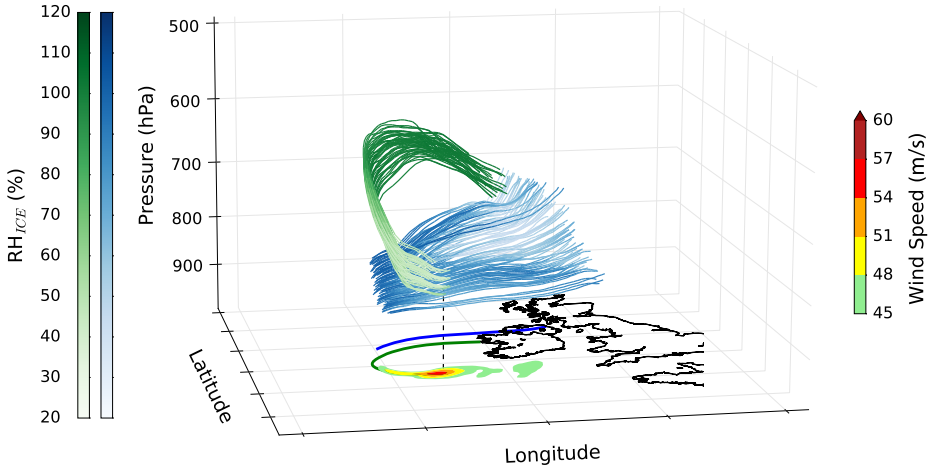

FIGURE 5 3D (lon–lat–pressure) view of SJ (green) and CCB (blue) airstreams from model simulations of windstorm *Tini* in a system-relative reference frame (trajectories from 2200 UTC on February 11 to 0700 UTC on February 12, 2014). Solid lines indicate the surface projection of the median trajectory for each of the airstreams. Earth-relative wind speed at 850 hPa (shading, m/s) at 0700 UTC (same as Figure 4a but only for wind speed above 45 m/s) is also shown [Colour figure can be viewed at wileyonlinelibrary.com]

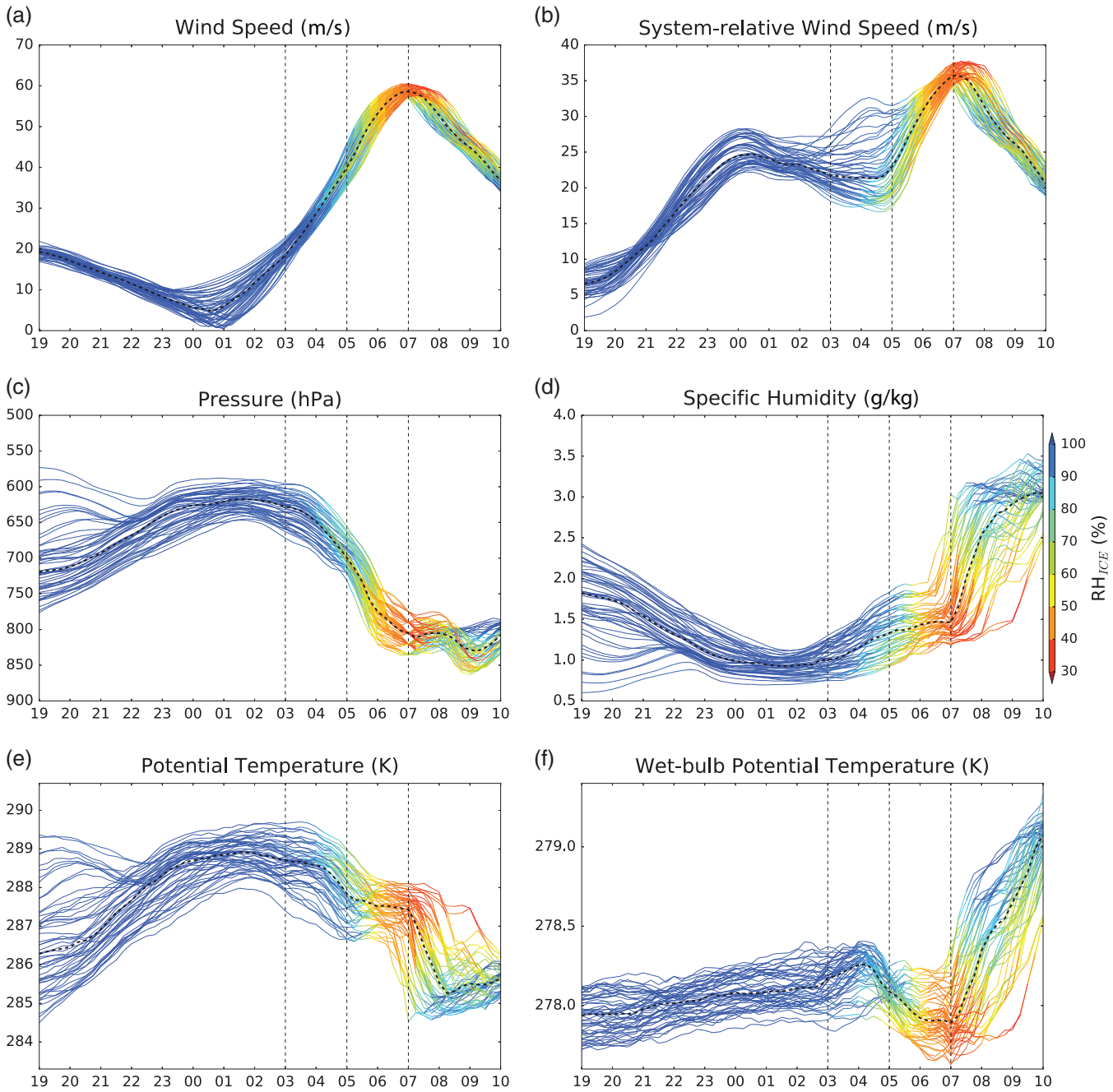

FIGURE 6 Time series (UTC) of (a) wind speed, (b) system-relative wind speed, (c) pressure, (d) specific humidity, (e) potential temperature, and (f) θ_w along SJ trajectories. Colours indicate RH_{ice} along trajectories. The dashed line indicates the median value of the field among the trajectories at each time [Colour figure can be viewed at wileyonlinelibrary.com]

Figure 6a shows the SJ undergoing a steady increase in Earth-relative speed, from $\lesssim$10 m/s at 0100 UTC to reaching up to 60 m/s at 0700 UTC. Part of this increase in speed is consistent with the fact that the airstream is rotating around the cyclone centre, moving eventually in the same direction of the overall motion of the storm (as previously said, *Tini* is moving at about 25 m/s). However, even in a system-relative reference frame, there is an increase in wind speed of about 15 m/s between 0500 and 0700 UTC (Figure 6b).

The descent of the SJ starts from about 650–600 hPa at around 0100–0300 UTC, but the bulk of the descent is between 0300 and 0700 UTC (Figure 6c) with a pressure increase of around 150 hPa in 3 hr. The descent is accompanied by a decrease in θ of about 1.5 K in total (Figure 6e). The increase in pressure results in a temperature increase of more than 15 K (not shown) and a consequent dramatic drop in RH_{ice} to around 40%. Nevertheless, the temperature stays well below zero during all the stages prior SJ descent. For this reason all relative humidities quoted are with respect to ice.

The decrease in θ during the first part of the descent shown in Figure 6e (from 0300 to 0500 UTC) is accompanied by an increase in specific humidity (Figure 6d) and can be attributed to evaporative cooling, primarily of condensate in the initial

cloud as confirmed by the decrease in cloud liquid water and ice observed just above the jet (not shown). The second part of the descent (after 0500–0530 UTC up to 0700 UTC), i.e. the most rapid part with the most of the system-relative wind speed increase, is instead characterized by almost constant θ and specific humidity. Hence, evaporative cooling did contribute to the initiation of descent by decreasing the buoyancy of the SJ air, but it did not contribute to the large final acceleration of the airstream.

Wet-bulb potential temperature is a conserved quantity in both dry and moist adiabatic flows. However, ice processes (i.e. freezing, melting, deposition and sublimation) contribute an additional latent heat and so can change θ_w (since θ_w is referred to liquid water). The time variations in θ_w are small, much smaller than those in θ, and hence difficult to evaluate reliably given possible errors in the trajectories (compare Figures 6e,f). The gradual increase in θ_w prior to about 0400 UTC), resulting in a total increase of less than 0.2 K, could well be the result of trajectory error, since the trajectories exist in a region of steep θ_w gradients. However, the rapid decline in θ_w during descent from 0400 to 0600 UTC (still amounting to only about 0.3 K) is consistent with a contribution from sublimation or melting of ice. We have not examined the precise contribution from different mechanisms, but the temperature increments due to cloud microphysics in the model (not shown) are in good agreement with θ_w variations, showing the same pattern of increase before 0400 UTC and decrease after. In comparison, contributions from radiation and other diabatic processes are negligible (not shown), confirming that the change in θ_w can be mainly associated with sublimation and melting processes. The size and nature of the variations in θ_w give us confidence that the trajectories are accurate enough for this study. The conservation properties were notably worse along trajectories derived using hourly model output, with variations of θ_w up to 2–3 K occurring during the SJ descent; this motivated our use of 15 min model output (section 2.2).

At the end of the descent (i.e. after 0700 UTC) the SJ reaches the top of the boundary layer and interacts with it. The speed on trajectories rapidly decreases, while θ_w increases abruptly by a few K. Shallow convection is visible in the simulated satellite imagery at this time, in the form of an arc-chevron cloud which may be related to the cloud patterns discussed by Browning and Field (2004). Of course, it is difficult to rely on the properties of trajectories undergoing such marked turbulent mixing, as they no longer represent a coherent airstream. This difficulty does not affect our study as we are primarily interested in the dynamics of generation and strengthening of the SJ and not in its interaction with the boundary layer after the descent, but it is worth noting that interaction with the boundary layer is clearly occurring after 0700 UTC.

To summarize, the set of trajectories traced back from the 850 hPa wind maximum satisfies the criteria required to identify this airflow as a SJ. The trajectories originated at mid-levels (650–600 hPa) inside the cloud head and descended rapidly (pressure increase of 150 hPa in 3 hr). They started out saturated, but adiabatic warming led to drying; a θ decrease during the first part of the descent is attributed to evaporative (and sublimation) cooling. During the final 2 hr of descent, the trajectories experienced an increase in system-relative wind speed of about 15 m/s.

3.3 | Evolution of mesoscale instabilities along the SJ

3.3.1 | Instability analysis

Having identified a SJ, we now evaluate the evolution of mesoscale instabilities on the airstream to test the hypothesis that the release of those instabilities had a role in driving descent and acceleration of the SJ (section 2.3 gives details of the method used).

Figure 7 shows the time–pressure profile of the airstream overlaid on bars representing the percentage of trajectories unstable to different instabilities at each time. In the hours prior to the SJ descent, while the air is saturated within the cloud head, there is a steady build-up of CSI in the airstream. This process continues until nearly 0400 UTC when >80% of the trajectories are labelled as unstable to CSI. This result is consistent with the findings of previous studies (Gray *et al.*, 2011; Baker *et al.*, 2014; Martínez-Alvarado *et al.*, 2014). As the descent begins, the number of CSI-unstable trajectories suddenly drops, primarily because the associated RH decreases to less than the threshold needed to label them as "CSI." In other words, while still perhaps conditionally unstable, the air is no longer actually unstable because it does not meet the saturation condition. Thus, while CSI release may be associated with the initial descent, it cannot explain the subsequent continued descent and acceleration when the airstream is outside the cloud head in a unsaturated environment.

However, Figure 7 also shows a rapid build-up of mainly dry mesoscale instabilities (i.e. SI and II, but with an additional relatively small contribution from CI) that lags the build-up of CSI by a few hours and reaches its maximum level at 0500 UTC, i.e. when the SJ descends more rapidly and strong acceleration starts to occur (after the initiation of descent related to the slight decrease in θ_w). A sudden drop in the number of unstable trajectories occurs during the descent, most of them changing to stable conditions by 0700 UTC, i.e. by the end of the SJ descent. II and SI are dry instabilities that do not need a saturated environment to be released and so can be released even when the airstream is out of the cloud head. Buckling of the saturated θ_w surfaces by the descending jet can create CI. Thus, the evolution of mesoscale instabilities appears to be closely related to the SJ descent and acceleration. Tracing of individual trajectories shows that the trajectories that initially become unstable to CSI are the same as those that become unstable to SI and II (not shown), suggesting the occurrence of a single process of destabilisation

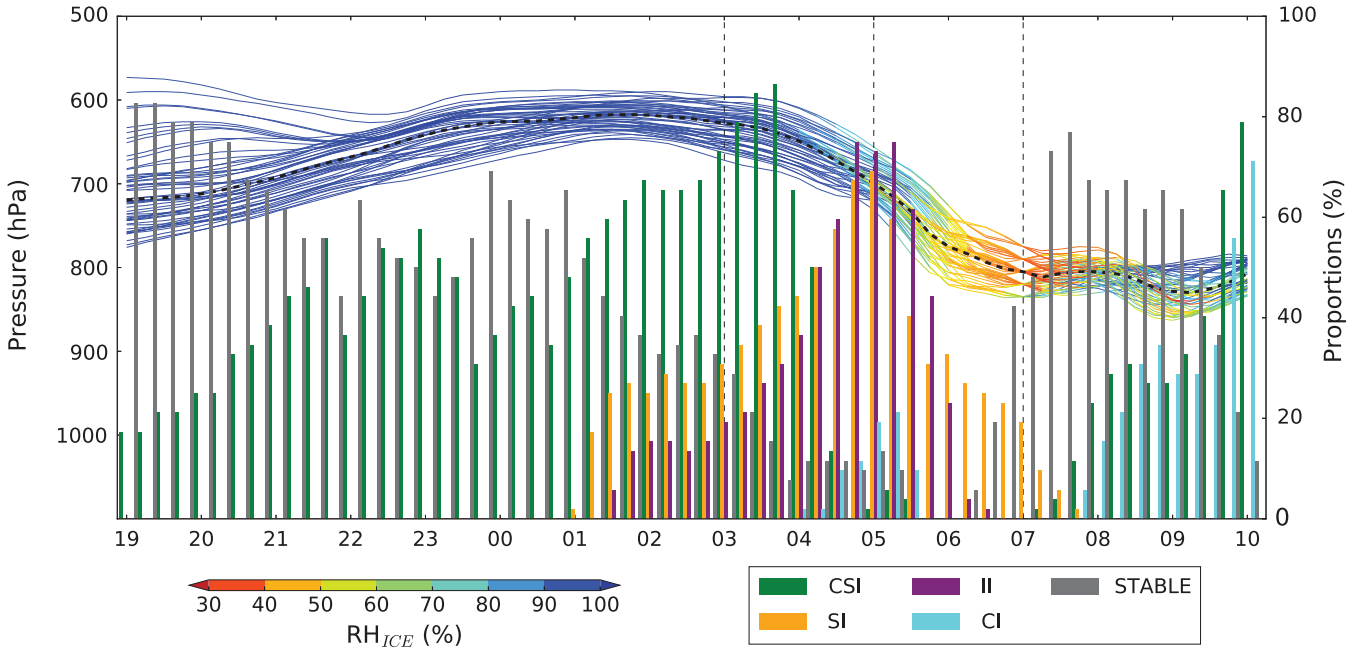

FIGURE 7 Time series (UTC) of pressure (colours indicate RH_{ice}) and diagnosis of instability conditions along SJ trajectories. The vertical bars indicate the fraction (proportion) of trajectories that are unstable to the different instabilities mentioned in the key table at the bottom of the figure and evaluated every 15 min (Table 1 gives the instability criteria). The dashed line indicates the median value of pressure among the trajectories at each time [Colour figure can be viewed at wileyonlinelibrary.com]

and subsequent release of mesoscale instability within the airstream. This behaviour implies rapid changes of PV (as SI is associated with PV< 0), with values becoming increasingly negative and then positive again in many of the trajectories between 0300 and 0700 UTC. Though mixing could possibly contribute to the decrease in PV, strong diabatic processes are clearly occurring in the cloud head. Mixing (parametrized or numerical) probably contributes to the increase to positive PV values (stable conditions) once the airstream reaches low levels (not shown).

3.3.2 | Vorticity structure

The condition used to label a trajectory as "II-unstable" is a negative vertical component of absolute vorticity ζ_z on pressure surfaces, while the condition to label it as "SI-unstable" is negative PV. Since static instability would rapidly lead to vertical mixing by the turbulence scheme, the behaviours of ζ_z and PV in the airstream are very similar. Figure 8 shows the horizontal and vertical patterns of ζ_z at two times during the evolution of the SJ.

Figure 8a shows ζ_z at 640 hPa and 0300 UTC. This is the pressure level where the SJ airstream was mainly located at this time and the time of the start of the SJ descent. The SJ cluster of trajectories (shown by black dots) is very small, around 40 km wide (Figure 8e,f), reinforcing previous research showing that high resolution is needed to represent the flow. Also, the trajectories are mainly confined to a small area of negative ζ_z just outside the main cyclonic branch of the system. Figure 8c shows that this negative ζ_z region is located between the 278 and 279 K θ_w contours, which have a gentle slope in the along-flow direction. A cross-section in the across-flow direction (Figure 8e) similarly shows the SJ located on one side of the negative ζ_z region. Two hours later (Figure 8b) the SJ has descended to 700 hPa. The SJ remains located in the small region of negative ζ_z, which is now more focused and intense (and still located between the 278 and 279 K θ_w contours, which are now much more sloped along the flow (Figure 8d,f)).

The along-flow cross-sections shown in Figure 8c,d show that the band of negative ζ_z is very narrow, forming part of a banded structure with strong positive ζ_z above and a second positive ζ_z band below which develops as the whole structure intensifies and becomes more slanted with time. Hence, the region with negative ζ_z travels with the SJ towards the tip of the cloud head, intensifying while retaining its shape and extension while at the same time descending and becoming more slanted. Moist isentropes simultaneously acquire a substantial slope along the flow (which is still within the 80% RH_{ice} contour). This narrow sloping banded structure is similar to that seen in observations made using the Doppler radar in an ana-cold-frontal zone which are described and attributed to mesoscale instability release by Browning *et al.* (2001). The across-flow cross-sections (Figure 8e,f) show that θ lines are also slanted in a radial direction. The band of negative ζ_z is located on the cold side of a frontal zone (bent-back front) and the buckling of θ_w lines is developing at 0500 UTC just below this region (and hence just below the SJ).

All these figures suggest that the growth of instability already highlighted in Figure 7 is a process taking place along the jet, in a Lagrangian sense.

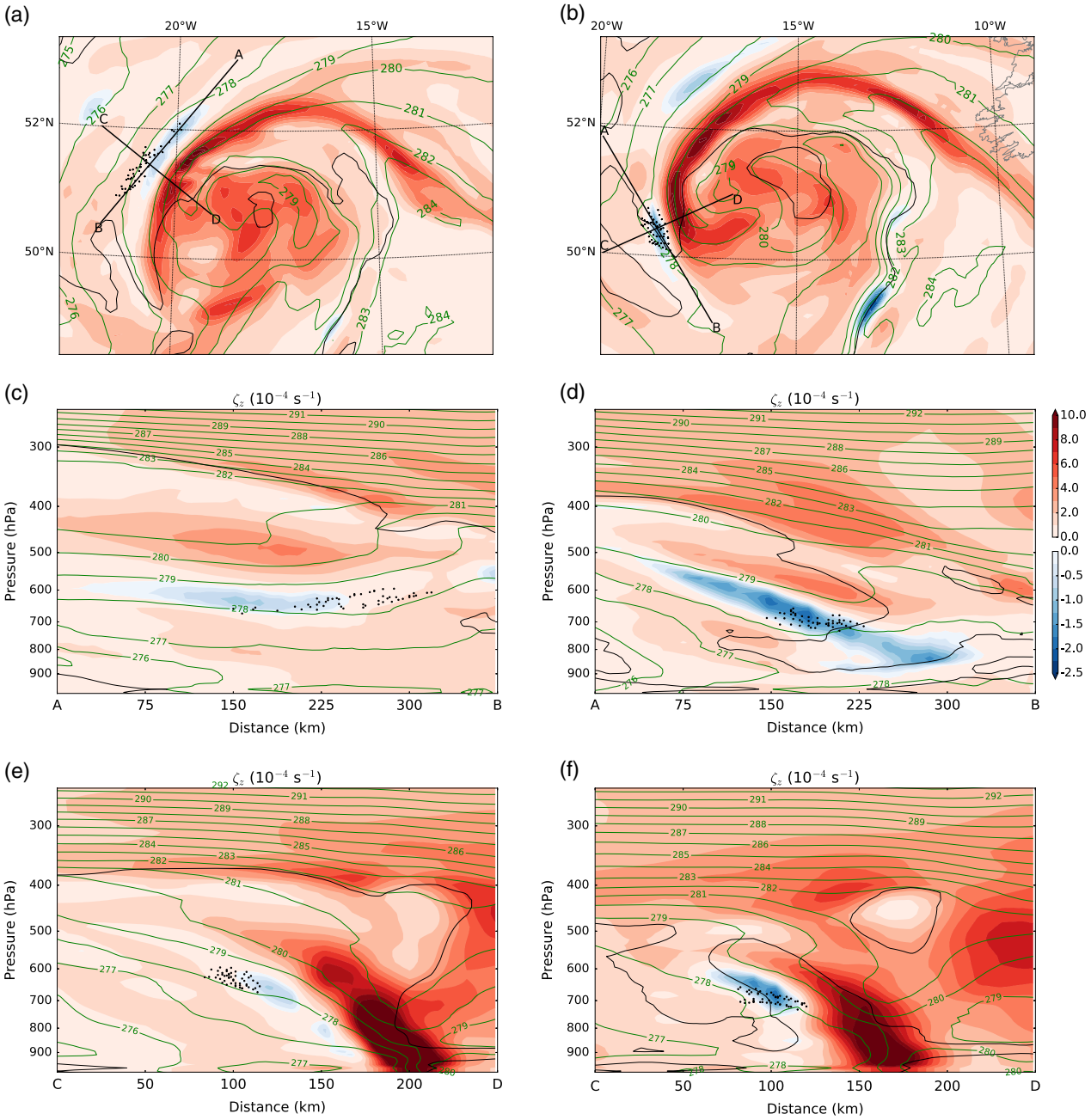

FIGURE 8 (a) Vertical component of absolute vorticity ζ_z (shading, $\times 10^{-4} s^{-1}$), θ_w (green contours, K) and cloudy regions (RH_{ice} =80%, black contours) at 640 hPa at 0300 UTC on February 12, 2014. (b) is as (a) but at 700 hPa at 0500 UTC on February 12, 2014. (c,d) Along-flow cross-sections of the same fields (transects AB in (a) and (b) respectively). (e,f) Across-flow cross-sections of the same fields (transects CD in (a) and (b) respectively). In (a) and (b) the dots show the locations of the SJ trajectories; in (c–f) dots show the projection of SJ trajectories onto the transect [Colour figure can be viewed at wileyonlinelibrary.com]

3.3.3 | Vorticity budgets

An analysis of the vorticity evolution equation has been performed along the trajectories and contributions of single terms to the overall changes in vorticity have been isolated to understand how the negative ζ_z values occurred. The vorticity equation on pressure levels is (Holton, 2004)

$$\frac{\partial \xi_z}{\partial t} + \mathbf{V}\cdot\boldsymbol{\nabla}\zeta_z + \omega\frac{\partial \xi_z}{\partial p} = \mathbf{k}\cdot\left(\frac{\partial \mathbf{V}}{\partial p}\times\boldsymbol{\nabla}\omega\right) - \zeta_z(\boldsymbol{\nabla}\cdot\mathbf{V}) + \text{friction}, \quad (1)$$

where ξ_z is the vertical component of relative vorticity. The first two terms on the right-hand side are respectively the tilting and stretching terms. In our analysis we consider the z-components to investigate the evolution of ζ_z. As we are evaluating all the terms on the trajectories, and so are in a Lagrangian reference frame, the advection term should not be considered. So, the only terms that can contribute to changes in ζ_z are tilting, stretching and friction.

Figure 9a shows a time series of ζ_z on the SJ trajectories. In the first hours the value of ζ_z is very close to 10^{-4} s^{-1}, i.e. the value of planetary vorticity in midlatitudes, indicating a very small ξ_z. A rather steady decrease in ζ_z occurs after 2300 UTC, with the majority of trajectories developing

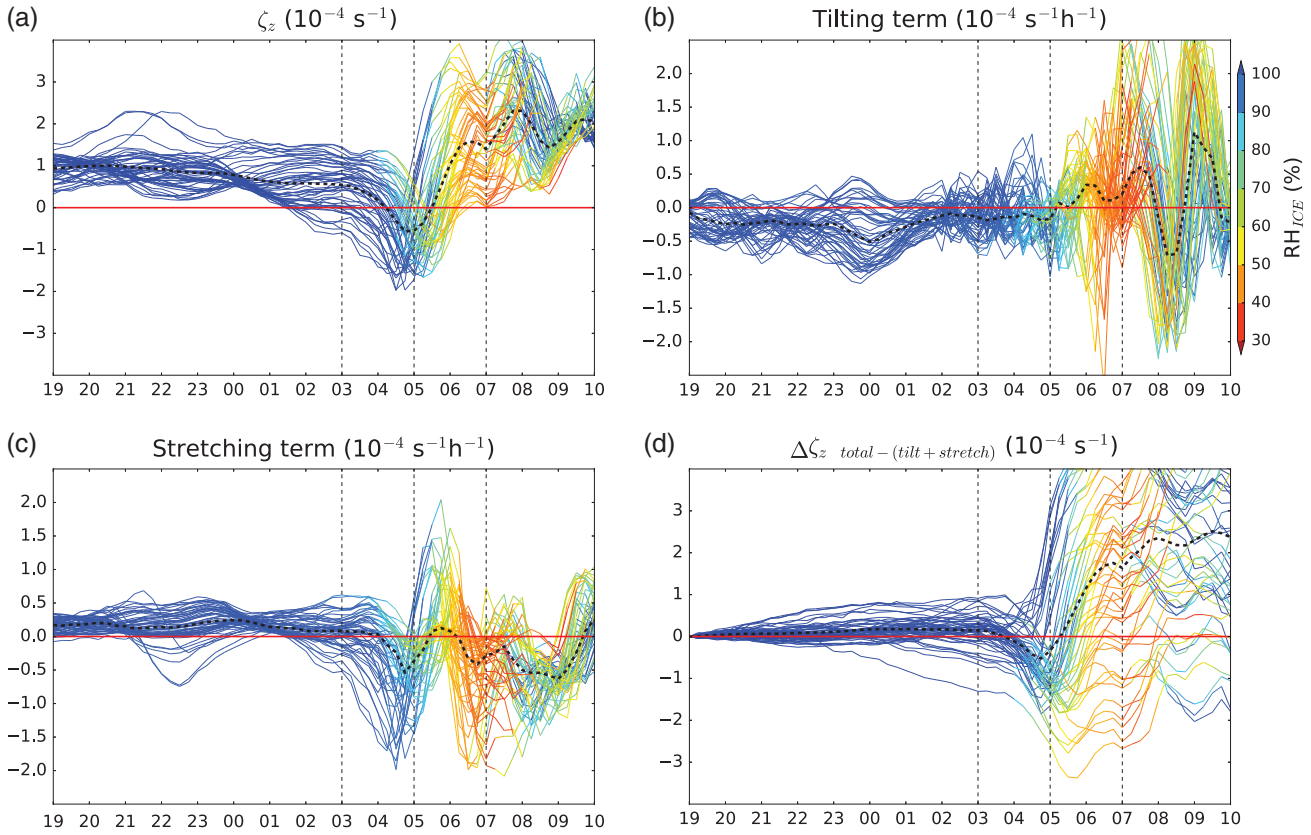

FIGURE 9 Time series (UTC on February 11–12, 2014) along SJ back-trajectories of (a) the vertical component of absolute vorticity ζ_z, (b) the tilting term in the vorticity equation, (c) the stretching term in the vorticity equation, (d) difference integrated over time between variations in ζ_z and the sum of tilting and stretching terms in the vorticity equation: $\Delta\zeta_{z\ \mathrm{total-(tilt+stretch)}}(t_1) = \zeta_z(t_1) - \zeta_z(t_0) - \int_{t_0}^{t_1}(\mathrm{tilting}(t) + \mathrm{stretching}(t))\,dt$. Colours indicate $\mathrm{RH_{ice}}$ along trajectories [Colour figure can be viewed at wileyonlinelibrary.com]

negative values around 0400–0500 UTC, implying II at the beginning of the SJ descent. After 0500 UTC, i.e. during the second part of the descent, a strong and sudden increase of ζ_z brings values well above zero, back to inertial stability.

Figure 9b shows that values of the tilting term are mainly negative around 0000 UTC, contributing to the initial decrease of ζ_z towards zero. During the following hours and up to 0500 UTC, the values of the tilting term remain negative, although closer to zero, for many of the SJ trajectories. Figure 9c shows that the stretching term is mostly negative between 0300 and 0500 UTC, the time when ζ_z becomes negative in the strongly descending SJ airstream. Figure 9d shows the difference between ζ_z and the increments due to the time integration of only the tilting and stretching terms. This time series demonstrates that tilting and stretching are causing much of the variations in ζ_z until the start of the descent, with values of $\Delta\zeta_{z\ \mathrm{total-(tilt+stretch)}}$ close to zero. This result implies that the contribution of the frictional term is negligible prior to this time. After 0400 UTC, part of the decrease in ζ_z on some trajectories is not accounted for by the tilting and stretching terms. After 0500 UTC, most significantly, all the trajectories show a strong increase in ζ_z that is not accounted for by the tilting and stretching terms.

Figure 7 shows the steady increase in the number of trajectories with negative ζ_z between 0300 and 0500 UTC, with Figure 8a,c highlighting that this is associated with a further decrease of the, already slightly negative, values of ζ_z in a localized region along the SJ airstream. During this stage the stretching term is negative for the trajectories that already have a negative ζ_z (not shown). This implies negative values of horizontal divergence on these trajectories (Equation 1). Horizontal convergence indeed occurs on a growing number of trajectories at this time. Figure 10a,b show that the stretching term and horizontal divergence are negative for almost all the SJ trajectories at 0500 UTC. As a result, the negative stretching term amplifies the magnitude of ζ_z on the trajectories whose values of ζ_z had already been brought below zero by the tilting term (i.e. the majority of the SJ trajectories by 0400–0500 UTC). Figure 10c,d show that horizontal vorticity is negative, both in its zonal and meridional components, on almost the entire jet at 0400 UTC. This is associated with a direct circulation occurring on the slantwise frontal zone along which the SJ travels. The negative values of tilting term at this stage indicate that part of this horizontal vorticity is converted into negative vertical vorticity while the SJ starts to be oriented downward.

The downward tilting of negative horizontal vorticity allows the generation of negative ζ_z along the jet, which is then amplified by a negative stretching term. This combined effect of tilting and stretching terms is sufficient to explain a large part of the decrease of ζ_z to negative values and thus the onset of II along the trajectories (cf. Figure 9d). Conversely,

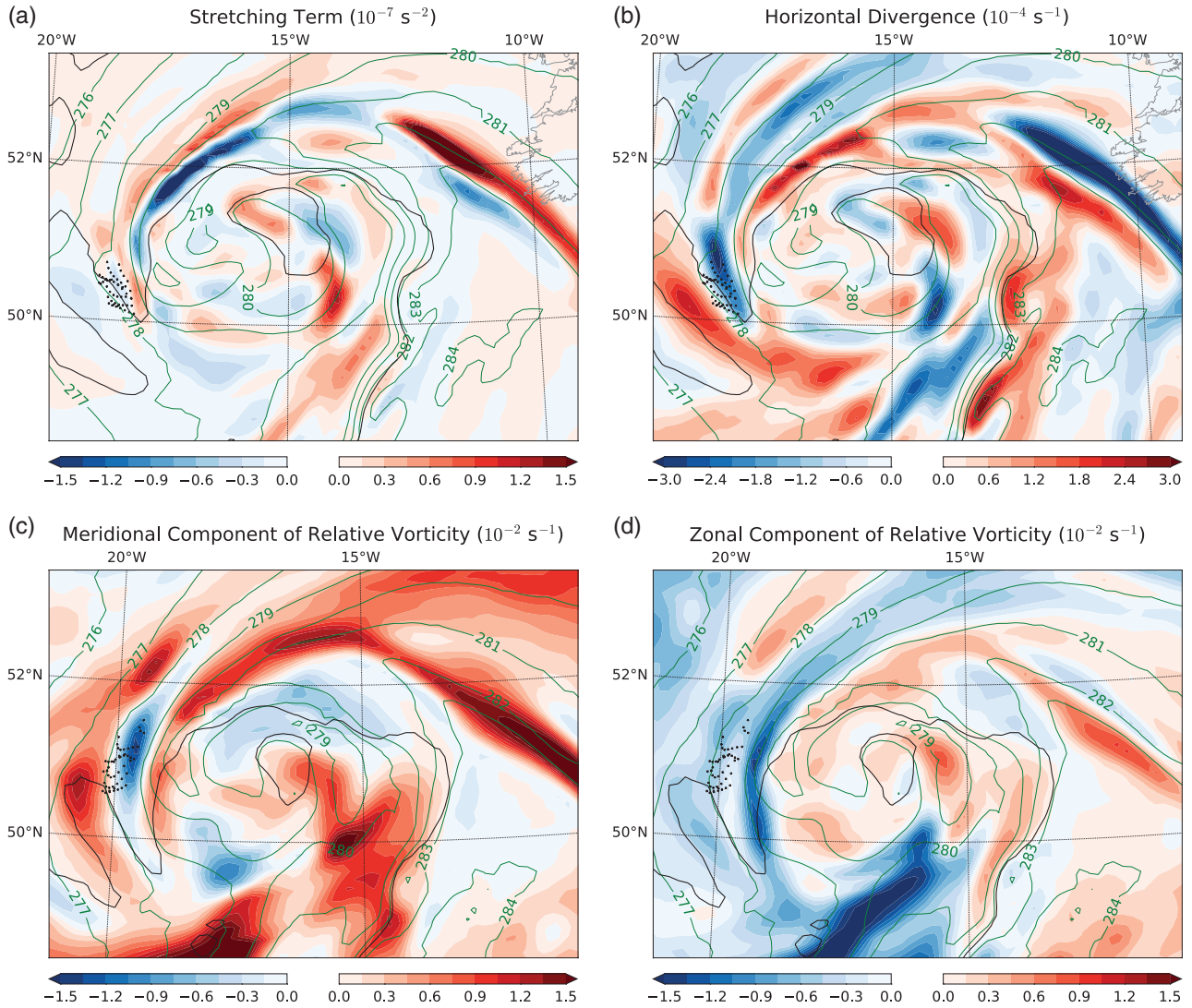

FIGURE 10 (a) Map of stretching term in the vorticity equation (shading), θ (green contours, K) and cloudy regions at 700 hPa (RH_{ice} =80%, black contour) at 0500 UTC with black dots showing the locations of the SJ trajectories. (b) is as (a), but for horizontal divergence. (c,d) are as (a) but for (c) meridional and (d) zonal components of relative vorticity at 655 hPa at 0400 UTC [Colour figure can be viewed at wileyonlinelibrary.com]

neither of these two terms is capable of explaining the sudden increase in ζ_z happening after 0500 UTC. This overall behaviour suggests that the steady evolution of the SJ airstream from stable to unstable is mainly explained by the tilting and stretching terms, while the process that brings it back to stable conditions is definitely not explained by those two terms. As stretching, tilting and friction are the only contributing terms in the equation, we can infer that "frictional" processes contribute to the rapid changes in vorticity after 0500 UTC. However, as will be discussed below, this corresponds to a period of folding and overturning of the flow and it seems likely that a significant contribution to this arises from numerical mixing between adjacent trajectories (i.e. small trajectory and interpolation errors in a rapidly changing environment). This can lead to mixing of vorticity – some trajectories apparently acquiring more negative vorticity from their neighbours and *vice versa* – but overall the genuine frictional forcing has a primary role in the removal of instability.

3.3.4 | Frontogenesis/frontolysis diagnostic

We conclude the analysis of the SJ airstream identified in the limited-area simulation by considering the evolution of frontogenesis. We use Petterssen's decomposition of frontogenesis (Petterssen, 1936), as utilised by Schultz and Sienkiewicz (2013):

$$F = \frac{d}{dt}|\nabla_H \theta| = \frac{1}{2}|\nabla_H \theta|(E\cos 2\beta - \nabla_H \cdot \mathbf{V}_H), \qquad (2)$$

where E is deformation and β the local angle between an isentrope and the axis of dilation (Keyser *et al.*, 2000, give more details). As mentioned in the Introduction, we expect to observe positive frontogenesis in correspondence with the main fronts (cold, warm and bent-back) and negative frontogenesis, i.e. "frontolysis," in the frontal-fracture region.

Figure 11a shows Petterssen frontogenesis on the 700 hPa pressure level at 0500 UTC (matching the time and level of Figure 8c). It broadly confirms the expected frontogenesis structure. However, a smaller-scale pattern is present at the tip of the cloud head, with small-scale horizontal banding taking

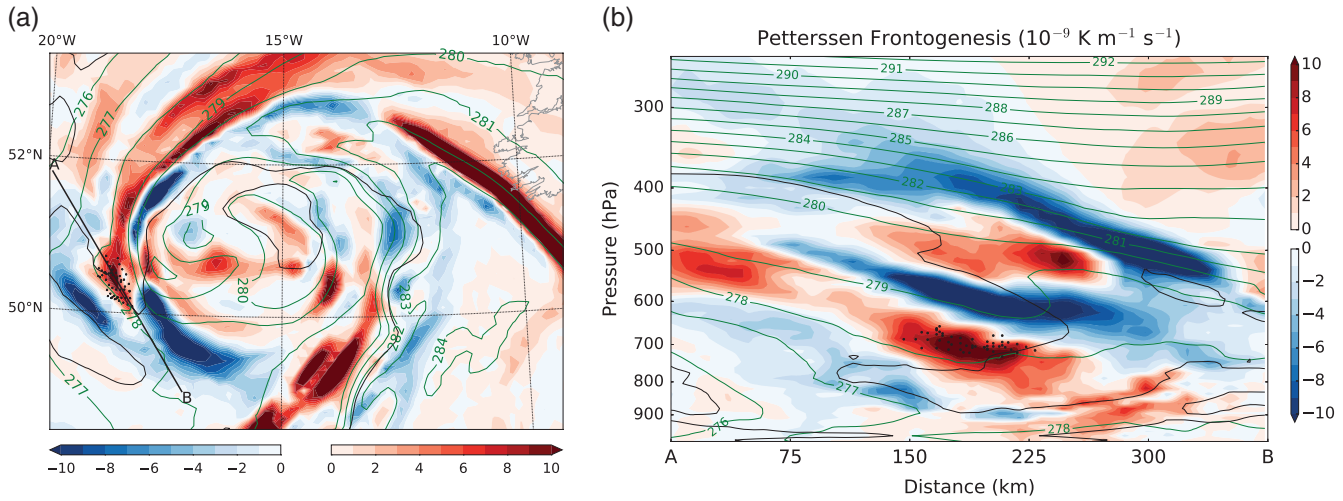

FIGURE 11 (a) Petterssen frontogenesis (shading), θ_w (green contours, K) and cloudy regions at 700 hPa (RH_{ice} =80%, black contours). (b) is as (a), but shown on a cross-section (transect AB in (a)). Both (a) and (b) are for 0500 UTC on February 12, 2014. In (a) the dots show the locations of the SJ trajectories, and in (b) the dots show the projection of SJ trajectories onto the transect [Colour figure can be viewed at wileyonlinelibrary.com]

place in a radial direction (i.e. passing through the location of the trajectories in the orthogonal direction to the marked cross-section). SJ trajectory points are located in a small region of positive frontogenesis (with a similar-sized region of frontolysis further out from the cyclone centre). The pattern of frontogenesis is well-correlated with the one of horizontal divergence described in section 3.3.3. The frontal-fracture region is an area of frontolysis and divergence while the SJ is enclosed in a localized (and time-intensifying) region of frontogenesis and convergence.

Figure 11b shows a cross-section through the SJ (matching the time and section of Figure 8d). This shows that bands of frontolysis and frontogenesis are slanted and piled vertically, very much like the ζ_z structure. There is clearly a process operating on a smaller scale than, and different from, the larger-scale frontogenesis/frontolysis pattern expected in the cloud head. We interpret this banding as arising from the slantwise motions previously discussed bending and distorting the θ field. (Although θ is not shown, note the distorted θ_w field in Figure 11b and in Figure 4c,d.) Frontogenesis is a kinematic quantity measuring Lagrangian tendency in the horizontal θ gradient, and it is difficult to interpret dynamically. However, we can certainly say that, while the broad structure of frontogenesis resembles that found in previous lower-resolution studies such as Schultz and Sienkiewicz (2013) and Slater *et al.* (2017), with widespread frontolysis in the frontal-fracture region, smaller-scale patterns related to the SJ motion are present at the tip of the cloud head and the SJ descent is certainly *not* associated (at least locally) with fontolysis.

3.4 | Comparison with a coarser-resolution model

3.4.1 | Motivation

In this section we analyse the impact of reducing the horizontal and vertical grid spacing. As discussed in section 2.1, previous studies have claimed that a horizontal grid spacing of around 10–15 km and a vertical grid spacing not larger than 200–300 m at SJ heights are required to correctly resolve the feature, both in case-studies (Clark *et al.*, 2005; Martínez-Alvarado *et al.*, 2010; Gray *et al.*, 2011; Smart and Browning, 2014) and idealized simulations (Baker *et al.*, 2014; Coronel *et al.*, 2016). The results of the previous sections in this article confirm that the SJ is a mesoscale feature, a narrow airstream whose dimensions are on the order of a few tens of km across and a few 100 m deep.

Here we investigate the consequence of reducing resolution by analysing the results from the global simulation that was used to initialize and drive the limited-area simulation. While we do not expect the coarser-resolution model to correctly resolve the SJ airstream, it is not obvious what the model solution will look like. For example, a 4 km grid spacing model cannot resolve deep convection as well as a 1 km grid spacing model, but in practice both will generate their own form of convection (e.g. Lean *et al.*, 2008). The question is, therefore, would we draw similar conclusions regarding mesoscale instabilities from a lower-resolution model (∼26 km horizontal and 170–350 m, at heights between 1 and 5 km, vertical grid spacing)?

Slater *et al.* (2017) also simulated windstorm *Tini*. Their simulation used a different model (the Advanced Research Weather and Forecasting Model version 3.4) and a different initial analysis and boundary conditions (the Global Forecast System 6-hourly, 0.5° analysis). It used a horizontal grid spacing of 20 km and 39 vertical levels, eight of which were below 850 hPa, and so was coarser in both dimensions than the one described in previous sections here and most similar to our global model simulation. Thus, while their simulation cannot be directly compared to ours, the similarity in resolution to our global model simulation means that it is worthwhile to note, *inter alia*, similarities to and differences from their simulations in the following.

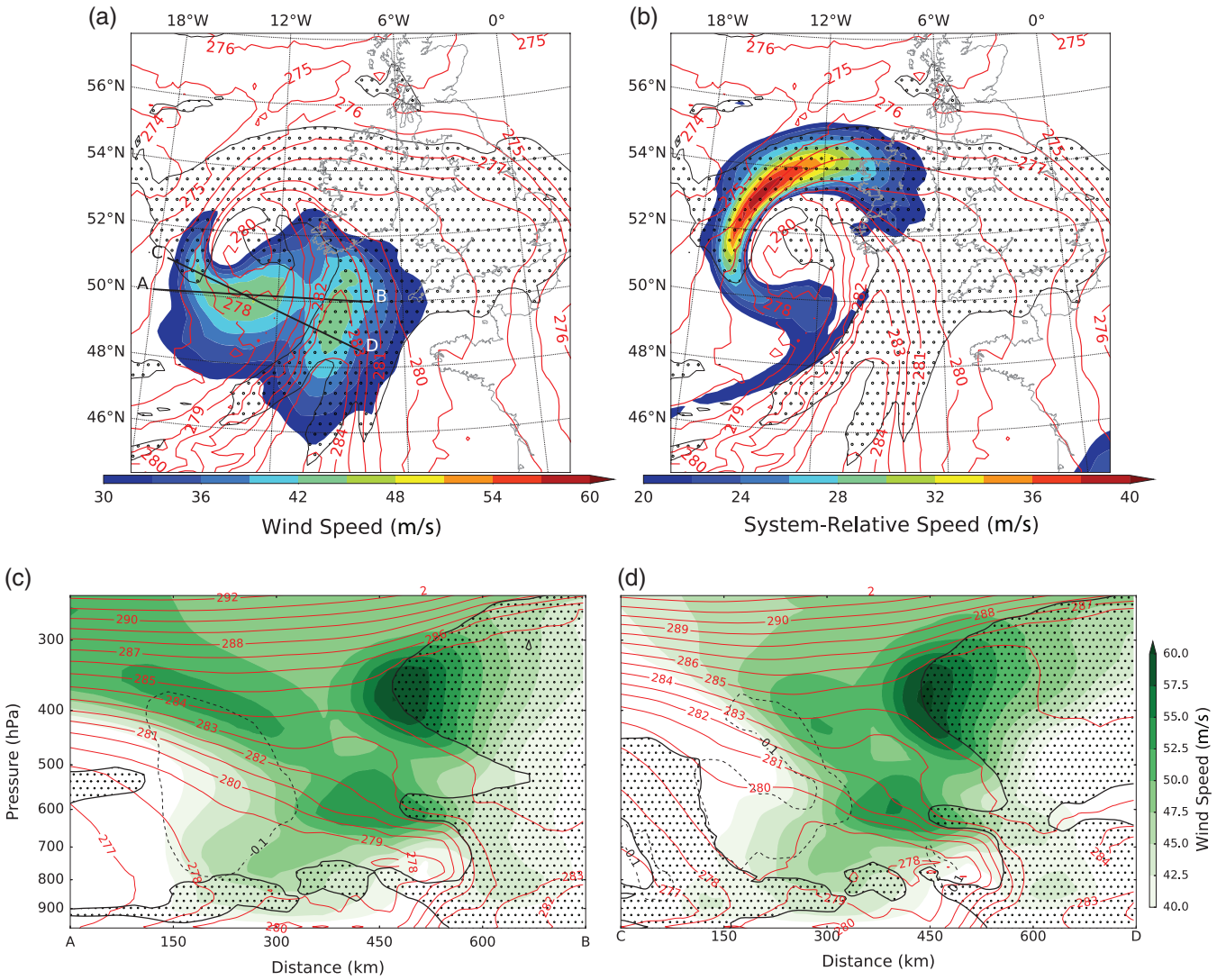

FIGURE 12 (a) Global model map of wind speed at 850 hPa (shading, m/s), θ_w at 850 hPa (K, red contours) and cloudy regions at 700 hPa (RH_{ice} >80%, black contour enclosing stippled regions). (b) is as (a), but with system-relative wind speed. (c,d) are cross-sections (transects AB and CD respectively in (a)) of wind speed (green shading, m/s), negative vertical velocity (dashed black contours, m/s), θ_w (red contours, K) and cloudy regions (RH_{ice} >80%, thick black contour enclosing stippled regions). All plots are for 0700 UTC on February 12, 2014 [Colour figure can be viewed at wileyonlinelibrary.com]

3.4.2 | Results

Figure 12 for the global model simulation is analogous to Figure 4 for the limited-area model simulation. The broad cyclone structure with clouds, fronts and strong-wind regions is very similar in the two simulations (compare Figure 12a with Figure 4a); however, some differences are evident. The wind maximum in the frontal-fracture region is broader in the coarser-resolution simulation, less focused and definitely weaker, with speed reaching only 48 m/s compared to 60 m/s in the higher-resolution simulation. In contrast, the WCB maximum speed is only slightly weaker at 45 m/s compared to 48 m/s. The system-relative winds in Figure 12b show a CCB that is similar in location and strength to the one in Figure 4b. This extends into the frontal-fracture region, but there is no suggestion of a local maximum where the SJ was identified in the higher-resolution model. Note also that the second band of cloud in the 12 km simulation which wraps around the cyclone centre outside the CCB is entirely absent from the lower-resolution simulation (Figure 12a,b).

The cross-sections shown in Figure 12c,d show many features in common with Figure 4c,d, but, again, the weakening of the low-level wind maximum in the frontal-fracture region is particularly evident. This low-level wind maximum is now weaker than the one in mid-levels. Moist isentropes are downward sloped and divergent in the frontal-fracture region, with no suggestion of folding, corresponding to a region of broad and weak descent. Note also that the two regions of slantwise descent (either side of the cloud) at the western end of Figure 4d are considerably weaker in Figure 12d. Figure 12c again highlights the absence of the second band of cloud which wraps around the cyclone centre outside the CCB.

The results from the global model simulation (which cannot resolve mesoscale instability release) show none of the key mesoscale features such as a separate wind maximum (and possibly multiple maxima), multiple slantwise

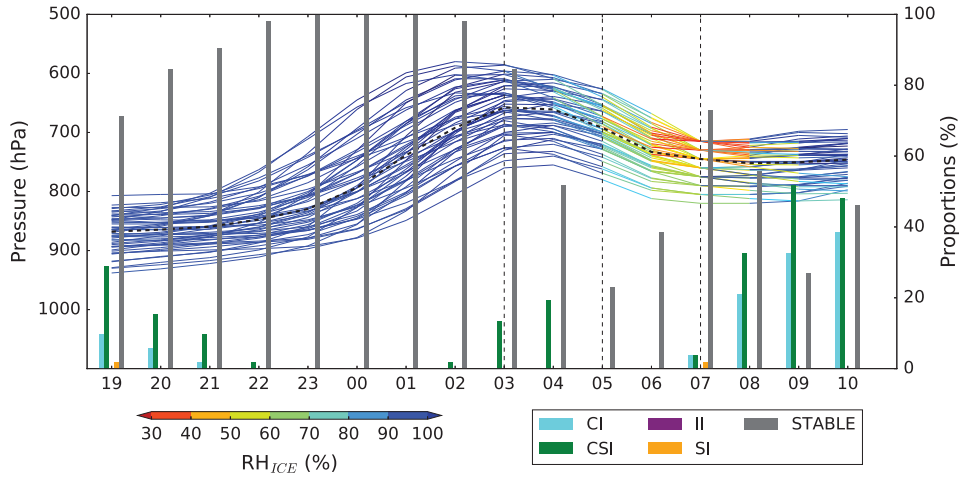

FIGURE 13 Global model time series (UTC) of pressure (colours indicate RH_{ice}) and diagnosis of instability conditions along SJ trajectories. The vertical bars indicate the fraction (proportion) of trajectories that are unstable to the different instabilities mentioned in the key table at the bottom of the figure and evaluated every 1 hr (Table 1 gives the instability criteria) [Colour figure can be viewed at wileyonlinelibrary.com]

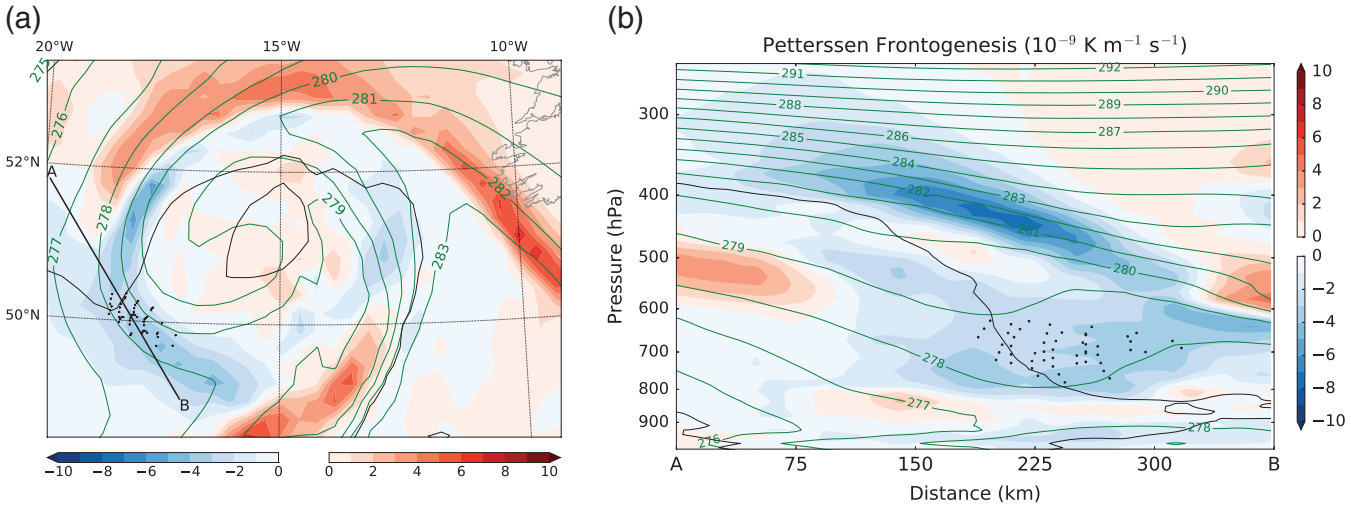

FIGURE 14 (a) Global model map of Petterssen frontogenesis (shading), θ_w (green contours, K) and cloudy regions at 700 hPa (RH_{ice} =80%, black contours). (b) is as (a), but showing a cross-section (transect AB in (a)). Both (a) and (b) are for 0500 UTC on February 12, 2014. In (a) the dots show the locations of the SJ trajectories, and in (b) the dots show the projection of SJ trajectories onto the transect [Colour figure can be viewed at wileyonlinelibrary.com]

descents, cloud bands and isentrope folding that are evident in the 12 km simulation. Rather they are thus consistent with a hypothesis that the relatively strong winds are caused by the synoptic-scale and frontal dynamics in the region superimposed on the storm motion with possible enhancement by mixing with high-momentum air from above.

The trajectory analysis was repeated for the strong winds in the frontal-fracture region. Although there is not a clear and focused wind maximum, grid points were selected with Earth-relative wind speed exceeding 47 m/s at 0700 UTC located at 760 hPa, or in contiguous levels above or below, as the best compromise to characterize the low-level strong winds. To refine the airstream, we kept only trajectories located at a pressure greater than 800 hPa at 1900 UTC and descending more than 50 hPa between 0400 and 0600 UTC. Figure 13 shows the time–pressure profile of these trajectories and the related instability bars. The overall motion of the airstream is quite different to that in the high-resolution simulation (Figure 7). There is a considerable reduction in instability along the trajectories than in the higher-resolution simulation, with most trajectories stable, though there is a weak signal of CSI at the time that the SJ starts descending. During the descent, the few trajectories with CSI lose this instability due to the reduction in RH associated with the descent. However, only about 20% are diagnosed as stable as the remaining trajectories still have negative MPV^* or N^2_m. The descent of these trajectories, although still steady and coherent, and occurring at the same stage of cyclone evolution as in the higher-resolution simulation, is much weaker.

Figure 14a shows the frontogenesis pattern (to be compared with Figure 11a). It shows frontogenesis in the inside flank of the cloud head and a broad area of frontolysis towards and into the frontal-fracture region, without any banding in the cloud head. The absence of strong banding is also evident in the cross-section shown in Figure 14b (to be compared with Figure 11b). There is much less fine-scale structure in these

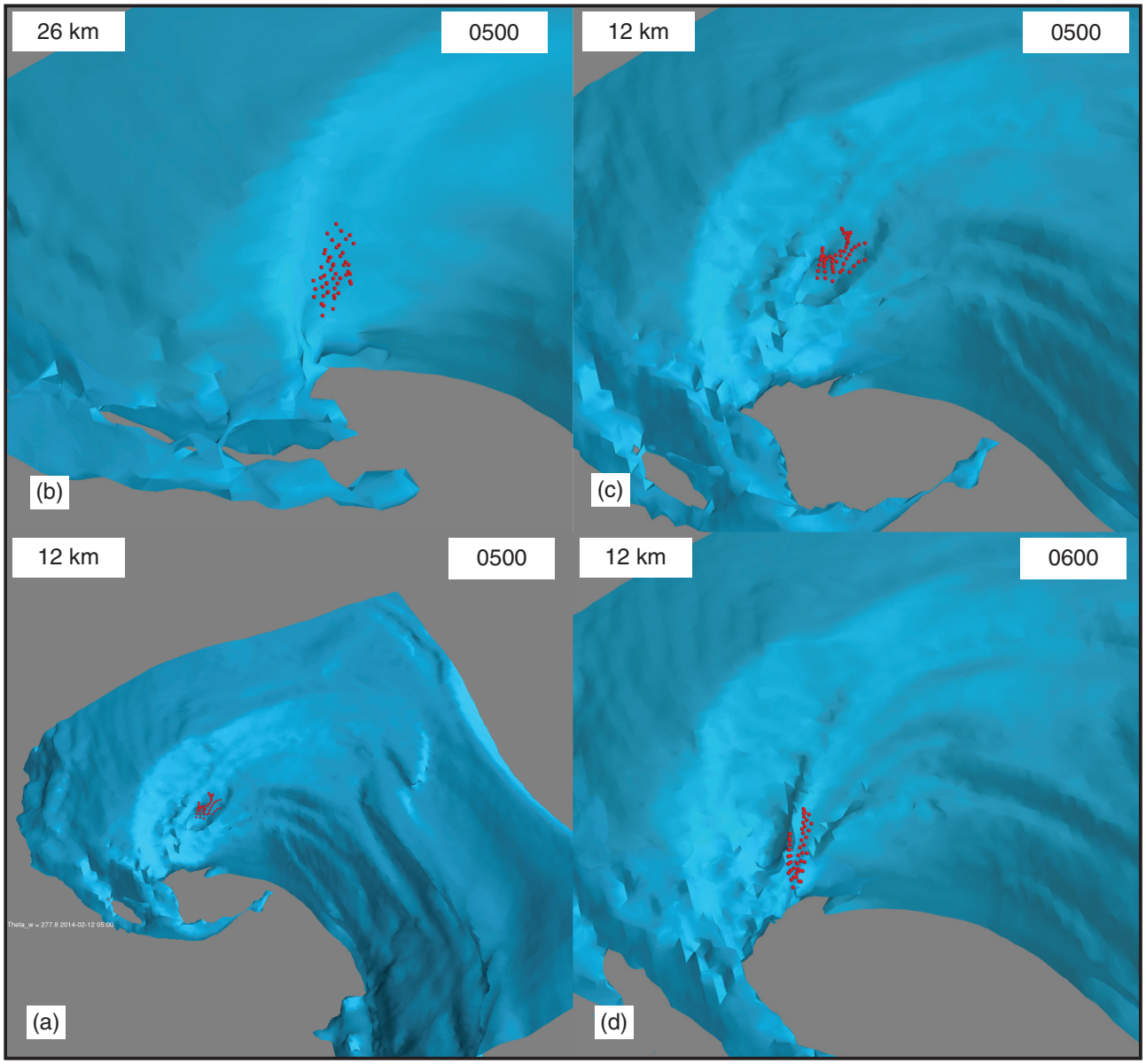

FIGURE 15 3D visualizations of simulated 277.8 K θ_w iso-surface and SJ trajectory locations (red dots). Clockwise from bottom left: (a) wider view of higher-resolution limited-area simulation run at 0500 UTC; zoomed-in views of (b) global model simulation at 0500 UTC, (c) and (d) higher-resolution limited-area simulation at 0500 and 0600 UTC, respectively, showing more clearly the θ_w surface folding (if present) in the vicinity of the SJ trajectories [Colour figure can be viewed at wileyonlinelibrary.com]

figures and the broad picture is very much in agreement with that shown in Schultz and Sienkiewicz (2013).

The difference in mesoscale structure between the high- and low-resolution simulations is highlighted in Figure 15a,b. These show three-dimensional visualizations of the 277.8 K θ_w surface, characteristic of the inner edge of the SJ, in both simulations at 0500 UTC, when the high-resolution SJ is about midway down its rapid descent. The SJ trajectory positions at this time are marked by red dots. Figure 15c,d zoom in on the high-resolution simulation at 0500 UTC, and 0600 UTC, as the SJ reaches the lowest point, but just before significant mixing occurs. Figure 15a,c show that the SJ is very closely related with a very localized region of rapid folding and overturning of the θ_w surface. Animations of the evolution, included in the supplementary information (Figures S2 and S3), make it very clear that this localized folding is very closely associated with the rapid plunge on the SJ into the frontal-fracture region. In contrast, the lower-resolution simulation shows no folding and, as already discussed, a gentler descent. Steepening of the θ_w surface does occur, and, using the high-resolution simulation as a guide, some hint of banding in this is noticeable, but overall the lack of mesoscale structure is striking.

To summarize, the airstream represented by the trajectories in the lower-resolution simulation has quite different characteristics to the SJ airstream observed in the higher-resolution simulation. This is not only a difference in wind speed: rather, these are two different airstreams with very different characteristics. Furthermore, as far as it is possible to compare, our lower-resolution results are similar to those found

by Slater *et al.* (2017). These results demonstrate that the lower-resolution model is capable of producing a weakly descending (and accelerating) airstream which has strong wind speed at lower levels and, by most criteria, might be classified as a SJ. However, this airstream has none of the characteristics exhibited by the much more focused and much stronger SJ diagnosed in the higher-resolution simulation; this SJ is associated with mesoscale instabilities which require the higher resolution to develop and be released.

4 | DISCUSSION AND CONCLUSIONS

The SJ is a phenomenon which has been studied in detail only in a relatively small number of, often relatively sparsely observed, extratropical cyclones. As a result, the dynamics producing a SJ are still a matter of debate. Indeed, the SJ has been defined based on its kinematic properties and it is not yet clear if a single mechanism is responsible for all SJs. Amongst those articles which broadly agree with the definition of a SJ used here, the primary question is the relative importance of larger-scale cyclone dynamics and mesoscale instabilities. This article has addressed this question applied to a SJ identified in the extratropical cyclone named windstorm *Tini*.

Windstorm *Tini* was a particularly intense and rapidly developing cyclone. The main tool used in this study was a limited-area simulation using the MetUM numerical weather prediction model. However, by chance the frontal-fracture region of the storm passed over the MST radar wind profiler at Aberystwyth and comparison with these data and other more routine observations suggests that the simulation reflects the key structures in the storm very well. A SJ has been identified in the simulation as a coherent airstream exiting from the cloud head, descending strongly (150 hPa in 3 hr) while accelerating into the frontal-fracture region and producing a strong and focused wind maximum close to 60 m/s. This airstream descends in an environment that is already broadly descending, with slanted θ_w surface that eventually fold on the same scale as the SJ. The θ_w range characteristic of the SJ is intermediate between those of the WCB and the CCB. Through most of its lifetime, the SJ has a horizontal extent around 40 km and a vertical extent of no more than 1 km.

The SJ has its own evolution which is clearly different to the one that the CCB undergoes. The SJ descent can be divided into two stages:

1. Strong descent accompanied by decrease in θ_w (cooling via sublimation) without system-relative acceleration;
2. Even stronger descent conserving θ_w and with large system-relative acceleration.

Mesoscale instabilities have been evaluated along the back-trajectories associated with the SJ. These show that the SJ becomes at first largely unstable to CSI and then to SI/II. The number of unstable trajectories associated with the SJ reaches a maximum as the SJ starts to descend; hence the descent of the SJ corresponds with the reduction of these instabilities and, by the time it reaches the top of the boundary layer, most of the instability has been released. At the same time, during descent, the horizontal system-relative wind speed increases by around 15 m/s.

The early stages of descent are most likely associated with the release of diagnosed CSI, but, as the descending airstream loses access to condensed water to evaporate or sublime, the airstream is no longer diagnosed as unstable to this process. However, by this time, the airstream is also unstable to SI. While it is very difficult to prove that the release of an instability causes the flow, this process of destabilisation and subsequent release (or removal) of mesoscale instability in the airstream can be strongly hypothesized to be affecting SJ dynamics.

The production of negative MPV^* and, ultimately, PV arises through diabatic heating and cooling in the cloud head. However, this manifests itself through the tilting of horizontal vorticity to produce negative ζ_z, which is then amplified before the final stage of descent by stretching. Chagnon and Gray (2009) similarly describe how stretching and tilting of background vertical (planetary) and horizontal vorticity (associated with vertical wind shear), respectively, can lead to relative vorticity (and so PV) dipoles. Figure 16 is a schematic showing the typical SJ trajectory, lying (as indicated by its later descent in the frontal-fracture region) in the intermediate θ_w region of the frontal zone, between strong ascent and descent. This is strongly forced by diabatic processes (primarily condensation and evaporation). The horizontal buoyancy gradient here generates horizontal vorticity (associated with the ascent and descent) along the SJ flow (i.e. helicity) which is subsequently tilted downwards when the SJ starts to descend (initially probably due to frontolysis). This therefore generates negative vertical vorticity. In this case we have identified that the buoyancy gradient is associated with the bent-back front but, of course, should there be multiple slantwise ascending/descending regions (e.g. associated with CSI), the same mechanism would apply.

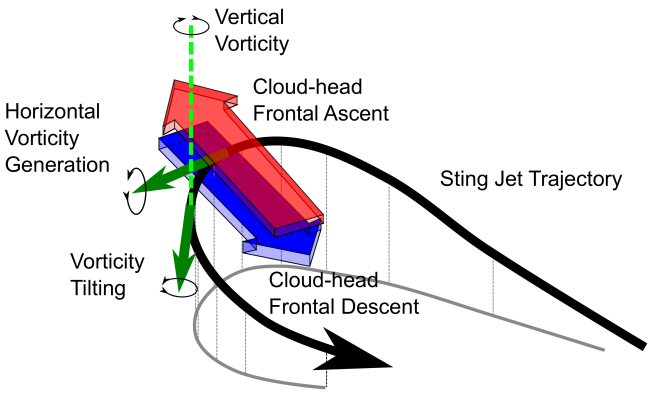

FIGURE 16 Schematic showing the generation of horizontal vorticity in the frontal zone and subsequent tilting along the SJ trajectory [Colour figure can be viewed at wileyonlinelibrary.com]

A slantwise-banded structure is present in ζ_z and the SJ travels towards the tip of the cloud head with a band of negative ζ_z which grows in amplitude while retaining its shape and extension while, at the same time, descending and acquiring a substantial slope. This banded structure is also shown in the frontogenesis field. Whereas the broad structure of frontogenesis resembles that already found in previous studies, with widespread frontolysis corresponding to the frontal-fracture region, smaller-scale patterns are present at the tip of the cloud head related to the SJ motion, and the small SJ region is actually associated with a local region of frontogenesis. On reaching the top of the boundary layer, ζ_z rapidly becomes positive. We assume that this largely reflects boundary-layer mixing, which is occurring in a cloudy boundary layer neutral or unstable to moist upright convection.

A lower-resolution simulation (with resolution coarser than that required to release mesoscale instabilities) also shows a region of relatively strong winds descending out of the cloud head. On its own, this would satisfy the definition of a SJ: the peak wind speed achieved in the jet is notably strong, around 48 m/s. However, the life history of the SJ in this lower-resolution simulation is in marked contrast to the flow observed in the higher-resolution simulation. The amount of descent is significantly less, so the peak wind speed does not reach the pressure level of 850 hPa (and barely reaches 800 hPa), and there is no clear wind maximum at 850 hPa. The SJ peak wind speed, while strong, is substantially weaker than the 60 m/s achieved in the SJ in the higher-resolution simulation, although the other main conveyor belts in the system are well represented and only marginally weakened by the lower resolution. The descent occurs in a region associated with frontolysis in the frontal-fracture region, and there is almost no indication of the generation and release of mesoscale instabilities, or of any associated folding of θ_w surfaces. The SJ in the lower-resolution simulation is entirely consistent with the hypothesis of strong winds caused by the frontal dynamics in the region: descent due to frontolysis into a region with high pressure gradient with flow aligned with the system motion. There is much less fine-scale structure in the frontogenesis field and the broad picture is in close agreement with what is shown by Schultz and Sienkiewicz (2013). The results from the lower-resolution simulation are similar to those found by Slater *et al.* (2017) and it is reasonable to suppose that this frontolysis-associated SJ, resulting from essentially balanced dynamics, is a relatively robust feature. Given that these authors ran a different model with different initial conditions, it is unknown whether a SJ of the nature found in our higher-resolution simulation would have formed if they had run the model with adequate resolution to enable it to do so.

Windstorm *Tini* has been demonstrated to be a valuable exemplar of intense SJ-containing extratropical cyclones. While wind-profiler observations provided valuable verification of the model simulations studied, the period of most interest occurred while the storm was still over the sea, thus removing complications due to surface orography. The formation and eventual release of a succession of mesoscale instabilities, from CSI through to SI and II, has been identified; this succession has been suggested, but not highlighted, in other studies. Furthermore, the suppression of the release, and even formation, of these instabilities in coarser-resolution models has been clearly demonstrated. These results have enabled us to draw the conclusion that these instabilities form in a background of (and probably enhanced by) synoptic and frontal dynamics which, in themselves, can lead to SJ-like structures, but that the release of these mesoscale instabilities can substantially enhance the final wind speed. Many of these features have been identified in other storms, but none has yet provided such a complete picture and, indeed, some features may not occur in all SJ cyclones.

To conclude, these results provide a valuable insight into the role of the various mechanisms that have been proposed for SJ formation. Concerning what we shall loosely denote as the "frontolysis" and "mesoscale instabilities" mechanisms, the results presented clearly demonstrate, for the first time to the authors' knowledge, that not "either/or" but "both" mechanisms can occur. Had diabatic processes not been strong enough to generate CSI/SI in windstorm *Tini*, a very strong wind would still have occurred in the frontal-fracture region and have been identified as a SJ. However, the CSI/SI that was generated led to a very substantial enhancement of this, both in strength (by 12 m/s) and in depth of descent. This increase in wind speed (in a region of already strong wind speeds) can lead to a large increase in associated damage since damage is typically considered to depend on wind speed cubed above a threshold (Leckebusch *et al.*, 2007; 2008). It is very difficult to separate the direct effect of the instability from modifications to the fontogenetic/frontolytic flow as stability decreases and, as concluded by Clark and Gray (2018), there is probably a continuum of behaviour from one extreme to the other. Nevertheless, in this case, the release of instability clearly had a qualitative effect on the flow.

A further lesson to be reinforced from this case (as has been stated in numerous past articles) is that it is essential that models are run with sufficiently high resolution to allow mesoscale instabilities to be released (and, it would seem in this case, to form) even if a SJ associated with frontolysis is evident in lower-resolution simulations. Weather forecasts of extratropical cyclone events containing SJs which are generated with insufficient model resolution will likely underestimate the associated wind risk. This finding has implications for medium-range (lead times of several days) weather warnings which are generated using global-domain models.

ACKNOWLEDGEMENTS

The authors are grateful to Michael Sprenger (IAC-ETHZ) for general support of the LAGRANTO code, and in particular

his development of an improved version allowing the input of sub-hourly data. The authors also wish to thank the Met Office for making the MetUM available and the National Centre for Atmospheric Science Computational Modelling Services for supporting the academic use of the MetUM on the UK National Supercomputing Service, ARCHER. This work was supported by the AXA Research Fund project "Sting Jet Windstorms in Current and Future Climates." The authors would also like to thank Gwendal Rivière and the two other anonymous reviewers for their valuable comments and Neil Hart for fruitful discussions and for his help with some of the figures.

REFERENCES

Arakawa, A. and Lamb, V.R. (1977) Computational design of the basic dynamical processes of the UCLA general circulation model. *Methods Computational Physics*, 17, 173–265.

Baker, L.H., Gray, S.L. and Clark, P.A. (2014) Idealised simulations of sting-jet cyclones. *Quarterly Journal of the Royal Meteorological Society*, 140, 96–110. https://doi.org/10.1002/qj.2131.

Bennetts, D.A. and Hoskins, B.J. (1979) Conditional symmetric instability – a possible explanation for frontal rainbands. *Quarterly Journal of the Royal Meteorological Society*, 105, 945–962.

Browning, K.A. (2004) The sting at the end of the tail: damaging winds associated with extratropical cyclones. *Quarterly Journal of the Royal Meteorological Society*, 130, 375–399.

Browning, K.A., Chapman, D. and Dixon, R.S. (2001) Stacked slantwise convective circulations. *Quarterly Journal of the Royal Meteorological Society*, 127, 2513–2536. https://doi.org/10.1002/qj.49712757803.

Browning, K.A. and Field, M. (2004) Evidence from meteosat imagery of the interaction of sting jets with the boundary layer. *Meteorological Applications*, 135, 663–680.

Browning, K.A. and Roberts, N.M. (1994) Structure of a frontal cyclone. *Quarterly Journal of the Royal Meteorological Society*, 120, 1535–1557. https://doi.org/10.1002/qj.49712052006.

Chagnon, J.M. and Gray, S.L. (2009) Horizontal potential vorticity dipoles on the convective storm scale. *Quarterly Journal of the Royal Meteorological Society*, 135, 1392–1408. https://doi.org/10.1002/qj.468.

Charney, J.G. and Phillips, N.A. (1953) Numerical integration of the quasi-geostrophic equations for barotropic and simple baroclinic flows. *Journal of Meteorology*, 10, 71–99. https://doi.org/10.1175/1520-0469(1953)010<0071:niotqg>2.0.CO;2.

Clark, P.A., Browning, K.A. and Wang, C. (2005) The sting at the end of the tail: model diagnostics of fine-scale three-dimensional structure of the cloud head. *Quarterly Journal of the Royal Meteorological Society*, 131, 2263–2292.

Clark, P.A. and Gray, S.L. (2018) Sting jets in extratropical cyclones: a review. *Quarterly Journal of the Royal Meteorological Society*. https://doi.org/10.1002/qj.3267.

Coronel, B., Ricard, D., Rivière, G. and Arbogast, P. (2016) Cold-conveyor-belt jet, sting jet and slantwise circulations in idealized simulations of extratropical cyclones. *Quarterly Journal of the Royal Meteorological Society*, 142, 1781–1796. https://doi.org/10.1002/qj.2775.

Davies, T., Cullen, M.J.P., Malcolm, A.J., Mawson, M.H., Staniforth, A., White, A.A. and Wood, N. (2005) A new dynamical core for the met office's global and regional modelling of the atmosphere. *Quarterly Journal of the Royal Meteorological Society*, 131, 1759–1782. https://doi.org/10.1256/qj.04.101.

Durran, D.R. and Klemp, J.B. (1982) On the effects of moisture on the brunt-väisälä frequency. *Journal of the Atmospheric Sciences*, 39, 2152–2158. https://doi.org/10.1175/1520-0469(1982)039<2152:oteomo>2.0.CO;2.

Edwards, J. and Slingo, A. (1996) Studies with a flexible new radiation code. Part I: choosing a configuration for a large-scale model. *Quarterly Journal of the Royal Meteorological Society*, 122, 689–719. https://doi.org/10.1002/qj.49712253107.

Forbes, R.M. and Clark, P.A. (2003) Sensitivity of extratropical cyclone mesoscale structure to the parametrization of ice microphysical processes. *Quarterly Journal of the Royal Meteorological Society*, 129(589), 1123–1148. https://doi.org/10.1256/qj.01.171.

Gray, S.L., Martinez-Alvarado, O., Baker, L.H. and Clark, P.A. (2011) Conditional symmetric instability in sting-jet storms. *Quarterly Journal of the Royal Meteorological Society*, 137, 1482–1500.

Gregory, D. and Rowntree, P.R. (1990) A mass flux convection scheme with representation of cloud ensemble characteristics and stability-dependent closure. *Monthly Weather Review*, 118, 1483–1506. https://doi.org/10.1175/1520-0493(1990)118<1483:amfcsw>2.0.CO;2.

Hart, N.C.G., Gray, S.L. and Clark, P.A. (2015) Detection of coherent airstreams using cluster analysis: application to an extratropical cyclone. *Monthly Weather Review*, 143, 3518–3531. https://doi.org/10.1175/MWR-D-14-00382.1.

Hart, N.C.G., Gray, S.L. and Clark, P.A. (2017) Sting-jet windstorms over the North Atlantic: climatology and contribution to extreme wind risk. *Journal of Climate*, 30, 5455–5471. https://doi.org/10.1175/JCLI-D-16-0791.1.

Hewson, T.D. and Neu, U. (2015) Cyclones, windstorms and the IMILAST project. *Tellus A*, 67, 27. https://doi.org/10.3402/tellusa.v67.27128.

Holton, J.R. (2004) *An Introduction to Dynamic Meteorology*, 4th edition. Cambridge, MA: Academic Press.

Keyser, D., Reeder, M.J. and Reed, R.J. (2000) A generalization of Petterssen's frontogenesis function and its relation to the forcing of vertical motion. *Monthly Weather Review*, 116, 762–780.

Lean, H.W. and Clark, P.A. (2003) The effects of changing resolution on mesocale modelling of line convection and slantwise circulations in FASTEX IOP16. *Quarterly Journal of the Royal Meteorological Society*, 129, 2255–2278. https://doi.org/10.1256/qj.02.57.

Lean, H.W., Clark, P.A., Dixon, M., Roberts, N.M., Fitch, A., Forbes, R. and Halliwell, C. (2008) Characteristics of high-resolution versions of the Met Office unified model for forecasting convection over the United Kingdom. *Monthly Weather Review*, 136, 3408–3424. https://doi.org/10.1175/2008MWR2332.1.

Leckebusch, G.C., Renggli, D. and Ulbrich, U. (2008) Development and application of an objective storm severity measure for the Northeast Atlantic region. *Meteorologische Zeitschrift*, 17, 575–587. https://doi.org/10.1127/0941-2948/2008/0323.

Leckebusch, G.C., Ulbrich, U., Frãhlich, L. and Pinto, J.G. (2007) Property loss potentials for european midlatitude storms in a changing climate. *Geophysical Research Letters*, 34, L05703. https://doi.org/10.1029/2006GL027663.

Lock, A.P., Brown, A.R., Bush, M.R., Martin, G.M. and Smith, R.N.B. (2000) A new boundary layer mixing scheme. Part I: scheme description and single-column model tests. *Monthly Weather Review*, 128, 3187–3199. https://doi.org/10.1175/1520-0493(2000)128<3187:anblms>2.0.CO;2.

Martínez-Alvarado, O., Baker, L.H., Gray, S.L., Methven, J. and Plant, R.S. (2014) Distinguishing the cold conveyor belt and sting jet air streams in an intense extratropical cyclone. *Monthly Weather Review*, 142, 2571–2595. https://doi.org/10.1175/MWR-D-13-00348.1.

Martínez-Alvarado, O., Weidle, F. and Gray, S.L. (2010) Sting jets in simulations of a real cyclone by two mesoscale models. *Monthly Weather Review*, 138, 4054–4075.

Matthews, T., Murphy, C., Wilby, R.L. and Harrigan, S. (2014) Stormiest winter on record for Ireland and UK. *Nature Climate Change*, 4, 738–740. https://doi.org/10.1038/nclimate2336.

NERC. (2017) *The NERC Mesosphere–Stratosphere–Troposphere (MST) radar facility at Aberystwyth [Hooper, D.]*. British Atmospheric Data Centre 2006–2017. Available at: http://badc.nerc.ac.uk/data/mst.

Parton, G.A., Vaughan, G., Norton, E.G., Browning, K.A. and Clark, P.A. (2009) Wind profiler observations of a sting jet. *Quarterly Journal of the Royal Meteorological Society*, 135, 663–680.

Persson, P.O.G. and Warner, T.T. (1993) Nonlinear hydrostatic conditional symmetric instability: implications for numerical weather prediction. *Monthly Weather Review*, 121, 1821–1833.

Petterssen, S. (1936) Contribution to the theory of frontogenesis. *Geofysiske Publikasjoner*, 11, 1–27.

Sanders, F. and Gyakum, J.R. (1980) Synoptic-dynamic climatology of the 'bomb'. *Monthly Weather Review*, 108, 1589–1606.

Schultz, D.M. and Browning, K.A. (2017) What is a sting jet? *Weather*, 72, 63–66. https://doi.org/10.1002/wea.2795.

Schultz, D.M. and Schumacher, P.N. (1999) The use and misuse of conditional symmetric instability. *Monthly Weather Review*, 127, 2709–2732.

Schultz, D.M. and Sienkiewicz, J.M. (2013) Using frontogenesis to identify sting jets in extratropical cyclones. *Weather and Forecasting*, 28, 603–613.

Shapiro, M.A. and Keyser, D. (1990) Fronts, jet streams and the tropopause. In: Newton, C. and Holopainen, E.O. (Eds.) *Extratropical Cyclones: The Erik Palmén Memorial Volume*. Boston, MA: American Meteorological Society, pp. 167–191.

Slater, T.P., Schultz, D.M. and Vaughan, G. (2017) Near-surface strong winds in a marine extratropical cyclone: acceleration of the winds and the importance of surface fluxes. *Quarterly Journal of the Royal Meteorological Society*, 143, 321–332. https://doi.org/10.1002/qj.2924.

Smart, D.J. and Browning, K.A. (2014) Attribution of strong winds to a cold conveyor belt and sting jet. *Quarterly Journal of the Royal Meteorological Society*, 140, 595–610. https://doi.org/10.1002/qj.2162.

Sprenger, M. and Wernli, H. (2015) The LAGRANTO Lagrangian analysis tool – version 2.0. *Geoscientific Model Development*, 8, 2569–2586. https://doi.org/10.5194/gmd-8-2569-2015.

Wernli, H. and Davies, H.C. (1997) A Lagrangian-based analysis of extratropical cyclones. I: the method and some applications. *Quarterly Journal of the Royal Meteorological Society*, 123, 467–489.

Wilson, D.R. and Ballard, S.P. (1999) A microphysically based precipitation scheme for the UK Meteorological Office Unified Model. *Quarterly Journal of the Royal Meteorological Society*, 125, 1607–1636. https://doi.org/10.1002/qj.49712555707.

Xu, Q. (1989) Frontal circulations in the presence of small viscous moist symmetric stability and weak forcing. *Quarterly Journal of the Royal Meteorological Society*, 115, 1325–1353. https://doi.org/10.1002/qj.49711549008.

SUPPORTING INFORMATION

Additional supporting information may be found online in the Supporting Information section at the end of the article.

How to cite this article: Volonté A, Clark PA, Gray SL. The role of mesoscale instabilities in the sting-jet dynamics of windstorm *Tini*. *Q J R Meteorol Soc*. 2018;144:877–899. https://doi.org/10.1002/qj.3264